

CONSTRAINTS ON THE INITIAL-FINAL MASS RELATION FROM WIDE DOUBLE WHITE DWARFS

JEFF J. ANDREWS¹, MARCEL A. AGÜEROS¹, A. GIANNINAS², MUKREMIN KILIC², SAURAV DHITAL³, SCOTT F. ANDERSON⁴
DRAFT May 23, 2022

ABSTRACT

We present observational constraints on the initial-final mass relation (IFMR) using wide double white dwarfs (DWDs). We identify 65 new candidate wide DWDs within the Sloan Digital Sky Survey, bringing the number of candidate wide DWDs to 142. We then engage in a spectroscopic follow-up campaign and collect existing spectra for these objects; using these spectra, we derive masses and cooling ages for 54 hydrogen (DA) WDs in DWDs. We also identify one new DA/DB pair, four candidate DA/DC pairs, four candidate DA/DAH pairs, and one new candidate triple degenerate system. Because wide DWDs are co-eval and evolve independently, the difference in the pre-WD lifetimes should equal the difference in the WD cooling ages. We use this to develop a Bayesian hierarchical framework and construct a likelihood function to determine the probability that any particular IFMR fits a sample of wide DWDs. We then define a parametric model for the IFMR and find the best parameters indicated by our sample of DWDs. We place robust constraints on the IFMR for initial masses of 2–4 M_{\odot} . The WD masses produced by our model for stars within this mass range differ from those predicted by semi-empirical fits to open cluster WDs. Within this mass range, where there are few constraining open cluster WDs and disagreements in the cluster ages, wide DWDs may provide more reliable constraints on the IFMR. Expanding this method to the many wide DWDs expected to be discovered by *Gaia* may transform our understanding of the IFMR.

Subject headings: binaries: general — white dwarfs

1. INTRODUCTION

Accurate mass measurements for large numbers of hydrogen-atmosphere (DA) white dwarfs (WDs), which dominate the WD population, became commonplace with the advent of spectroscopic surveys such as the Palomar-Green Survey (Green et al. 1986) and the Sloan Digital Sky Survey (SDSS; York et al. 2000). These confirmed that the DA mass distribution is strongly peaked at 0.6 M_{\odot} (e.g., Kepler et al. 2015). However, matching these final WD masses to initial, zero-age-main-sequence masses is challenging, and large uncertainties about which main-sequence stars evolve into which WDs are still the norm. For example, the data cannot accurately tell us which stars produce those 0.6 M_{\odot} DAs, with estimates ranging from 1.0 to 2.5 M_{\odot} (Weidemann 2000). This implies that predictions for mass loss as stars evolve into 0.6 M_{\odot} WDs can differ by $>1 M_{\odot}$.

Sweeney (1976) pioneered the most commonly used method for constraining the initial-final mass relation (IFMR). The cooling age (τ_{cool}) of a WD in an open cluster is derived from spectroscopy, and this age is subtracted from the cluster’s age to determine the WD progenitor’s main-sequence lifetime. Using stellar evolution codes, this lifetime is converted into an initial mass M_i ; paired with its spectroscopically determined mass, this M_i then provides a constraint on the IFMR (e.g., Weidemann & Koester 1983; Weidemann 2000).

In practice, this method is often difficult to implement:

¹ Department of Astronomy, Columbia University, 550 West 120th St., New York, NY 10027, USA

² Department of Physics and Astronomy, University of Oklahoma, 440 West Brooks St., Norman, OK, 73019, USA

³ Embry-Riddle Aeronautical University, 600 South Clyde Morris Blvd., Daytona Beach, FL 32114, USA

⁴ Department of Astronomy, University of Washington, Box 351580, Seattle, WA 98195, USA

the open clusters must have accurate ages, member WDs must be identified and separated from contaminating objects, and these often faint WDs must be observed with high-resolution spectrographs. Furthermore, most accessible open clusters are $\lesssim 600$ Myr old, so that only stars with $M_i \gtrsim 3.5 M_{\odot}$ have evolved into WDs (there has been some recent work to identify WDs in older clusters; e.g., Kalirai et al. 2008, 2014).

Finley & Koester (1997) used a different approach. The co-eval WDs in the wide double WD (DWD) PG 0922+162 can be considered to have evolved independently. By comparing the more massive WD to massive WDs with accurate M_i determinations in open clusters, these authors assigned PG 0922+162B a M_i of 5.5–7.5 M_{\odot} . Adding the corresponding main-sequence lifetime to the massive WD’s τ_{cool} , Finley & Koester (1997) derived a system age of $\approx 320 \pm 32$ Myr. Finally, these authors calculated the pre-WD lifetime of the less massive WD by subtracting its τ_{cool} from the system age, and, using stellar evolution codes, found $M_i = 3.8 \pm 0.2 M_{\odot}$ for this WD. The uncertainty on this point in the initial-final mass plane is comparable to that for the best open cluster data.

While promising, this study has not been widely replicated. Until recently, there were only ≈ 35 known wide DWDs, and many were poorly characterized. Most lacked spectra, and even those with spectra were ill-suited to this analysis because of large uncertainties in their τ_{cool} . Furthermore, it has not been clear how to convert observations into robust constraints on the IFMR.⁵

⁵ We have found three other instances where this method was applied to a wide DWD. It was first used by Greenstein et al. (1983) on Gr 576/577, but one of the WDs in this pair is composed of an unresolved double degenerate (Maxted et al. 2000). Because of the potential for mass transfer within the unresolved binary system,

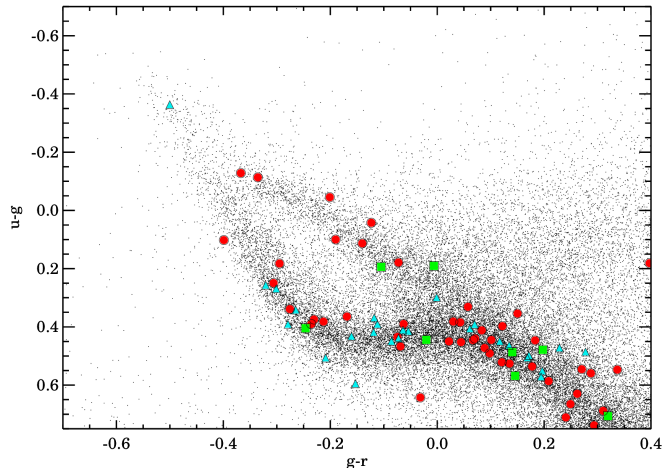


FIG. 1.— $(u - g)$ versus $(g - r)$ for $\approx 4 \times 10^4$ SDSS objects with $\sigma_{ugr} < 0.15$ mag, $\sigma_{iz} < 1.0$ mag, $\mu > 35$ mas yr $^{-1}$, and $\sigma_{\mu} < 10$ mas yr $^{-1}$. The plot boundaries define the box in color space within which we sought to identify new WDs. The sickle-shaped band corresponds to the DA cooling sequence, with hotter, younger WDs toward the upper left, and cooler, older WDs toward the bottom right. The width of the band is primarily due to variations in the DA masses: for example, WDs slightly more massive than the canonical $0.6 M_{\odot}$ have slightly higher surface gravities, and therefore slightly bluer $(u - g)$. The band of objects with bluer $(u - g)$ for a given $(g - r)$ is the cooling sequence for non-DA WDs. Hot DB WDs lie at the upper left of this band; as they cool to $\lesssim 12,000$ K they appear as DC WDs with featureless blackbody spectra. The red circles are the candidate WDs in 23 new candidate wide DWDs identified here; the green squares are candidate WDs in four additional new candidate systems, while the cyan triangles are the WDs in the 13 known systems we re-detect.

In this work, we develop a statistical model that allows any well-characterized wide DWD to constrain the IFMR. We first construct a likelihood function to determine the probability that any particular IFMR fits a sample of wide DWDs, while taking into account observational uncertainties by marginalizing over the underlying parameters from the observables. We then develop a four-parameter piecewise-linear model for the IFMR, and iterate over the model parameters using a Markov Chain Monte Carlo technique to find the best parameters indicated by our wide DWDs.

In Andrews et al. (2012, hereafter Paper I) we presented the results of a search for new DWDs in the SDSS Data Release 7 (DR7; Abazajian et al. 2009). Here, we begin by describing in Section 2 the results of a search for DWDs in the larger SDSS Data Release 9 (DR9; Ahn et al. 2012). We assemble a catalog of 142 candidate and confirmed DWDs that includes new systems, those found in Paper I and in the literature, and those recently published by Baxter et al. (2014). In Section 3, we discuss our spectroscopic follow-up observations of a subset of WDs in these binaries, and present the results of our model fits to these spectra. In Section 4, we revisit the Finley & Koester (1997) result and develop our hi-

this is not a good system for constraining the IFMR. Girven et al. (2010) applied the method to PG 1258+593 to constrain the initial mass of its magnetic companion SDSS J130033.48+590407.0. While of use for studying the origin of magnetic WDs (e.g., Dobbie et al. 2012), this is another instance where the system does not place useful constraints on the IFMR. Recently, Catalán (2015) developed her own form of this method. Although promising, it has generated meaningful constraints for only four systems so far.

erarchical Bayesian model. We test our model on mock data, then apply it to a well-characterized subset of wide DWDs. In Section 5 we discuss our resulting constraints on the IFMR; we conclude in Section 6.

2. SEARCHING FOR WIDE DWDs

2.1. Common Proper Motion Pairs

We first search for DWDs by matching proper motions of WD candidates in SDSS, which requires accurate photometry and astrometry. Although the SDSS Data Release 8 is nearly triple the size of the DR7 photometric catalog, the astrometric solutions are not calibrated against the USNO CCD Astrograph Catalog data (Zacharias et al. 2004), causing a systematic shift of ≈ 50 mas yr $^{-1}$ (Munn et al. 2008). DR9, however, includes an expanded photometric catalog and improved astrometric solutions (with a precision of a few mas yr $^{-1}$), which allowed us to expand the search for DWDs described in Paper I. From the $> 9 \times 10^8$ primary photometric objects in DR9, we selected those classified as stars (`pctype` = 6) and matching our photometric and proper motion (μ) quality constraints ($\sigma_{ugr} < 0.15$ mag, $\sigma_{iz} < 1.0$ mag, $\mu > 35$ mas yr $^{-1}$, $\sigma_{\mu} < 10$ mas yr $^{-1}$).

In Paper I, we used the color-color regions defined by Girven et al. (2011) to identify WDs in $(u - g)$ versus $(g - r)$ space (the regions are shown in Figure 4). To include helium-atmosphere DB WDs in this search, we used a more liberal color constraint, selecting those stars with $-0.7 < (g - r) < 0.4$ and $-0.7 < (u - g) < 0.75$. Figure 1 shows the $(u - g)$ versus $(g - r)$ colors of the $\approx 4 \times 10^4$ SDSS objects that met our quality constraints and fell within this region of color space.

Quasars (QSOs) are by far the biggest contaminant in this region of color-color space. Munn et al. (2004) found that requiring $\mu > 10$ mas yr $^{-1}$ eliminated 95% of QSOs with $r < 20$ mag. Our $\mu > 35$ mas yr $^{-1}$ criterion should eliminate nearly all QSOs. Contaminating main-sequence stars and halo subdwarfs (metal-poor, Population II main-sequence stars) are more difficult to remove, as these objects may overlap with WDs in color and may have $\mu > 35$ mas yr $^{-1}$. As shown in Kilic et al. (2006), however, WDs can be effectively separated from blue stars in a reduced proper motion (H_r) diagram.⁶

Figure 2 is H_r versus $(g - i)$ for the objects in our sample. Because of their smaller radii, WDs are clearly separated from main-sequence stars and halo subdwarfs. We used the dashed line in Figure 2, adapted from Smith et al. (2009), to separate halo subdwarfs from WDs, thereby reducing our sample to $\approx 34,000$ objects.

Next, we searched for common proper motion matches within these data. We defined a match as occurring when two WDs had an angular separation $\theta < 5'$, and, following Dhital et al. (2010), that their proper motions have a matching parameter $\Sigma^2 < 2.7$. Among our $\approx 34,000$ objects, we thus identify 57 candidate DWDs.

Some of these candidate pairs may contain WDs at different distances and with different radial velocities, which, when projected on the sky, happen to result in

⁶ $H_r = r + 5 \log \mu + 5$.

⁷ $\Sigma^2 = (\Delta\mu_{\alpha}/\sigma_{\Delta\mu_{\alpha}})^2 + (\Delta\mu_{\delta}/\sigma_{\Delta\mu_{\delta}})^2$, where $\Delta\mu$ is the difference in μ measured in right ascension (α) and declination (δ), and σ_{μ} is the error in μ .

$\Sigma^2 < 2$. Since the probability of finding a randomly aligned pair depends on the volume of phase space being searched, the random alignment likelihood should scale linearly with θ , and a critical θ should separate pairs more likely to be real from those more likely to be contaminants. In Paper I, we found that pairs with $\theta < 1'$ are most likely real. However, because our selection criteria have changed, we re-estimate this critical θ .

Figure 3 shows a clear excess in the number of candidate pairs with $\theta < 100''$. We determine a linear fit to the distribution of systems with $\theta > 100''$, those that are most likely to be random alignments. Extrapolating this fit to those pairs with smaller θ suggests that $\lesssim 2$ of the systems with $\theta < 100''$ are likely to be random alignments. We conclude that the 36 pairs with $\theta < 100''$ are high-probability DWD candidates (13 are re-detections of previously known systems).

The likelihood of random alignments drops dramatically as μ becomes larger. We therefore also searched for pairs with $\mu > 80 \text{ mas yr}^{-1}$, requiring only that $\Sigma^2 < 10$. We identified an additional four pairs in this manner, bringing the total number of newly identified candidate common proper motion DWDs to 27.

2.2. Astrometrically Close Pairs

The population synthesis simulations described in Paper I predicted that the population of wide DWDs should have a minimum orbital separation of a few 10^2 AU. At typical distances to photometrically identified WDs, this corresponds to $\theta \approx 1''$, within the resolving limit of SDSS photometry. There should therefore be a substantial population of wide DWDs in SDSS with $\theta \leq 7''$, the

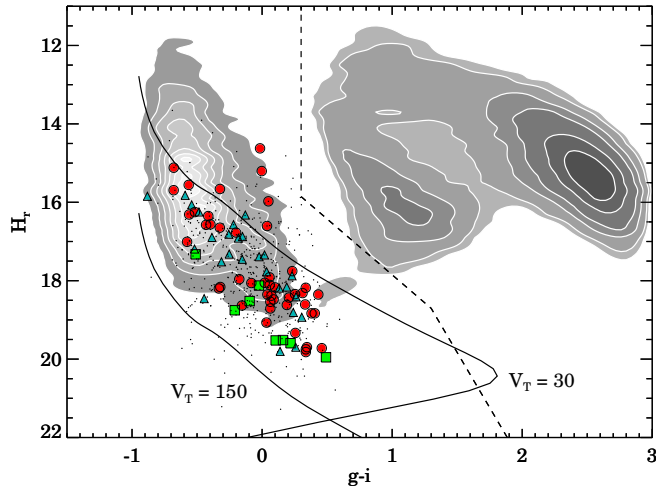


FIG. 2.— Reduced proper motion H_r versus $(g-i)$ for the objects in Figure 1. The locus at $(g-i) \approx 2.5$ is of main-sequence stars, while that at $(g-i) \approx 1$ is of halo subdwarfs. The spectroscopically confirmed WDs in the Kleinman et al. (2013) SDSS catalog with a measured μ are shown by the contours peaking at $(g-i) \approx -0.5$. We used the dashed line, adapted from Smith et al. (2009), to separate halo subdwarfs from candidate WDs. The solid lines represent the locations of WDs for transverse velocities $V_T = 30 \text{ km s}^{-1}$ (corresponding to the disk population) and 150 km s^{-1} (the halo population), and show that our candidates are likely in the Galactic disk. The symbols are the same as in Figure 1. Our candidates have systematically larger H_r because we require that they have relatively large μ and because the SDSS photometric catalog extends to fainter magnitudes than the spectroscopic catalog used by Kleinman et al. (2013) to identify WDs.

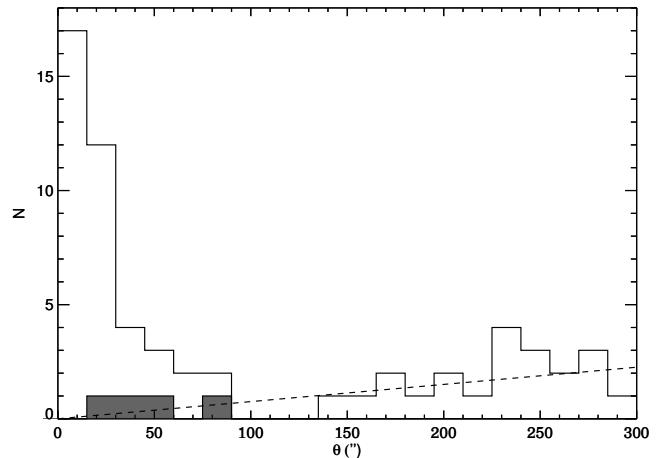


FIG. 3.— Angular separation (θ) distribution of our candidate common proper motion DWDs. The four pairs with $\Sigma^2 > 2$ but $\mu > 80 \text{ mas yr}^{-1}$ are shown in gray. The probability that a given pair is due to a random alignment should increase roughly linearly with θ . The dashed line shows the best fit line to the distribution beyond $100''$, where the noise dominates, assuming $N(\theta) \propto \theta$ and that the line goes through the origin. Extrapolating this fit to smaller θ suggests that pairs with $\theta < 100''$ are real pairs, while pairs at larger θ are physically unassociated.

minimum separation identifiable through proper motion matching to the USNO-B photometric plates. Can these pairs be identified through other means?

Dhital et al. (2015) search for photometrically resolved pairs of low-mass stars in SDSS with small θ . These authors identify $> 40,000$ binaries with θ of $0''.4-10''$ and argue that wide pairs can be efficiently identified without having to match proper motions. Similarly, Baxter et al. (2014) identified a set of wide DWDs with $\theta \lesssim 30''$ in DR7 based exclusively on photometry.

To identify such pairs in DR9, we again started with the photometric catalog and extracted a sample of candidate WDs. Since μ measurements are generally unavailable for objects with nearby companions in SDSS, halo subdwarfs and QSOs are now significant sources of contamination. To reduce the contamination due to halo subdwarfs, we applied a more stringent color-color cut to our sample, selecting only those objects in the photometric catalog that fall in the Girven et al. (2011) DA WD region (cf. discussion in Paper I).

Girven et al. (2011) estimated that 17% of the objects falling within this color-color region are QSOs. However, this was based on a $g < 19$ mag sample of objects with SDSS spectra. Our sample extends to $g = 21$, and we expected QSOs to be a more significant contaminant.

To determine the extent of the overlap between QSOs and WDs, we examined the distribution in $ugrizHK$ color space of spectroscopically confirmed SDSS QSOs (Schneider et al. 2010) and WDs (Kleinman et al. 2013). While QSOs and WDs can be cleanly separated using SDSS+infrared colors (see bottom right panel of Figure 4), the majority of the SDSS photometric catalog lacks UKIDSS counterparts and infrared photometry.⁸

⁸ The UKIRT Infrared Deep Sky Survey (UKIDSS) project is defined in Lawrence et al. (2007). UKIDSS uses the UKIRT Wide Field Camera (WFCAM; Casali et al. 2007). The photometric system is described in Hewett et al. (2006), and the calibration is described in Hodgkin et al. (2009). The pipeline processing and

Of the *ugriz* color-color pairings, the least overlap between QSOs and WDs occurs in $(u - g)$ versus $(g - r)$. The bottom panels of Figure 5 show that, in this color combination, the number of QSOs falling in the Girven et al. (2011) region increases at fainter magnitudes, but primarily at redder $(g - r)$. In addition to using the Girven et al. (2011) color-color regions to identify candidate WDs, for objects with $g > 18$ we added the additional requirement that $(u - g) < -0.1$. There are 67,640 objects in DR9 that satisfy these photometric constraints.

We searched for pairs of objects within this sample with $\theta < 2'$, removing pairs within crowded fields. Figure 6 is a histogram of the resulting θ distribution. For $\theta \gtrsim 20''$, the rate of matches increases linearly with θ , as expected for random alignments. We fit a line through the origin to the θ distribution for pairs with $\theta > 50''$. When extrapolating to smaller θ values, the line suggests that $\lesssim 5$ of the systems with $\theta < 10''$ are likely to be random alignments. Accordingly, we selected the 43 pairs with $\theta < 10''$ as high-confidence candidate DWDs. Five of these were previously known, so that we have 38 new candidate DWDs.

Among the previously known wide DWDs are the 11 systems identified in Paper I and 36 systems identified elsewhere in the literature. To that sample we add 27 systems identified by common proper motions and 38

identified by their small astrometric separations. Baxter et al. (2014) found 53 wide DWDs in SDSS and spectroscopically confirmed 26 of these (one additional pair was found to be a contaminant). Thirty of the 53 DWDs are new, and 11 of these are spectroscopically confirmed. In Table 2 we provide positions, g magnitudes, and μ_α and μ_δ , when available, for the combined catalog of 142 candidate and confirmed wide DWDs, including the 19 candidate and 11 spectroscopically confirmed pairs from Baxter et al. (2014).

2.3. Comparison with Previous Samples

Figure 7 shows μ versus θ for our new DWDs, as well as for pairs from the literature, including the Baxter et al. (2014) DWDs. Our pairs are very different from those in the literature, and in particular from the DWDs identified by Baxter et al. (2014), despite similar source catalogs (SDSS DR9 here, DR7 for Baxter et al. 2014).

These differences are largely due to the search methods employed: Baxter et al. (2014) initially used a less restrictive color-color region to select photometric WD candidates. These authors then searched for candidate wide DWDs by finding nearby pairs of blue objects without proper motion matching, similar to the astrometric

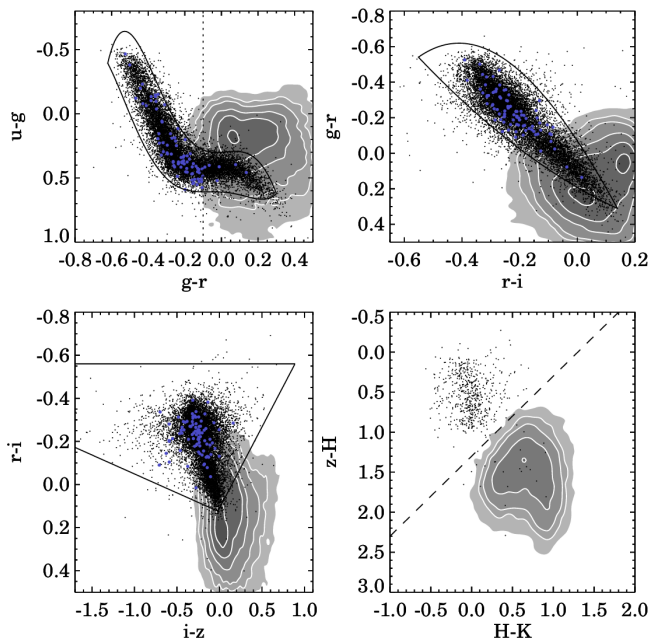


FIG. 4.— Distribution in color space of spectroscopically confirmed QSOs (contours) and WDs (black dots) from SDSS (Schneider et al. 2010; Kleinman et al. 2013). The Girven et al. (2011) WD regions are overplotted. Blue dots indicate WDs from the 43 candidate wide DWDs that pass the selection criteria described in Section 2.2. The objects in both SDSS catalogs with UKIDSS (Lawrence et al. 2007) counterparts are also plotted in $(z - H)$ versus $(H - K)$ in the bottom right panel. The dashed line in that panel is $(z - K) = 1.3$ mag. While this line cleanly separates WDs from QSOs, the majority of our candidate WDs lack UKIDSS counterparts. Using SDSS photometry alone, $(u - g)$ versus $(g - r)$ colors provide the best constraints to separate QSOs from WDs.

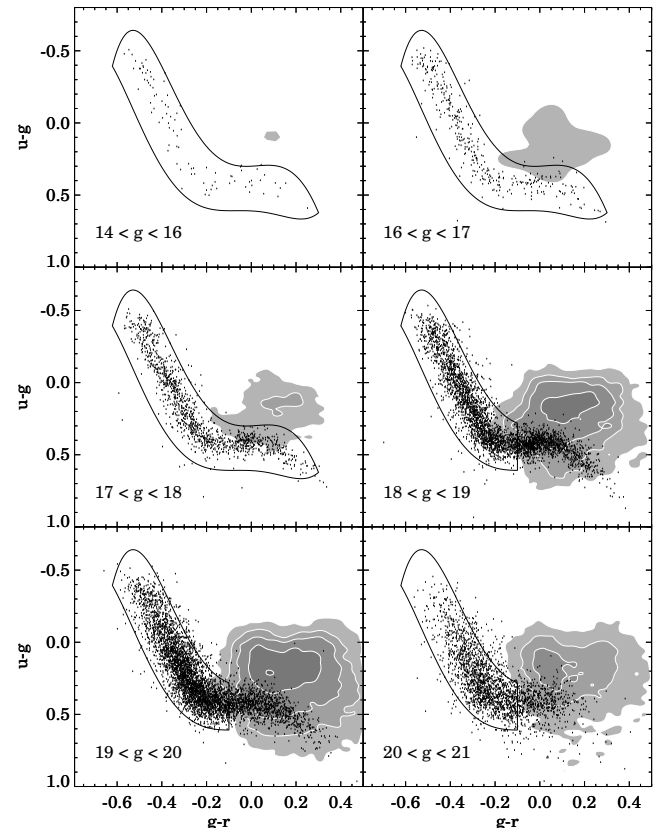


FIG. 5.— $(u - g)$ versus $(g - r)$ for photometrically identified candidate WDs binned by magnitude. The contours are the spectroscopically confirmed QSOs from the Schneider et al. (2010) catalog, while the solid line in the top two and middle left panels is the Girven et al. (2011) WD region. QSOs become a major source of contamination at fainter magnitudes and redder $(g - r)$. To identify fainter candidate WDs, we therefore added the constraint that for $g > 18$ mag, $(g - r) < -0.1$, resulting in the regions described by the solid line in the middle right and bottom two panels.

science archive are described in Hambly et al. (2008). We used the Eighth Data Release.

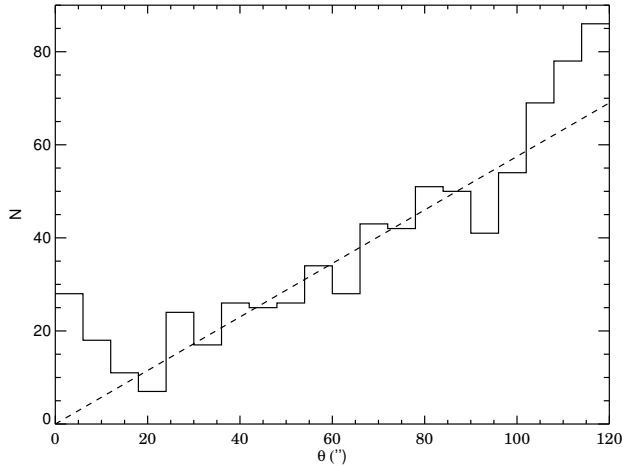


FIG. 6.— Angular separation distribution for astrometrically selected candidate DWDs. For $\theta \gtrsim 20''$, the number of matches increases linearly with θ , as expected for random alignments. The dashed line shows the best fit line to the distribution of random alignments beyond $50''$ where random alignments dominate, again assuming $N(\theta) \propto \theta$ and that the line goes through the origin. Extrapolating this fit to smaller θ shows that pairs with $\theta < 10''$ are excellent candidates for follow-up.

approach described above. Compared to our candidates, these candidate DWDs have smaller θ and μ values. But the small overlap between the two samples argues for the value of both approaches.

We recover all of the new wide DWDs found in Paper I in this search. Another 21 wide DWDs from the literature fall within the SDSS DR9 footprint; we recover eight of these pairs. The reasons we fail to re-detect the other 13 DWDs are given in Table 1. Most are not recovered because one or both of the WDs are cool enough to have colors too red to fall within our WD photometric region. This suggests that our detection algorithm is insensitive to the wide DWDs that contain cooler WDs, but these WDs have such large τ_{cool} that they are less useful for constraining the IFMR than the hotter WDs we do find.

3. ASSEMBLING A SPECTROSCOPIC SAMPLE

3.1. Observations and Reductions, and Spectra From the Literature

Identifying a large number of DWDs is only the first step toward constraining the IFMR. While the WDs' effective temperatures (T_{eff}) can be derived from SDSS photometry to within a few 100 K, typical SDSS photometric errors are large enough to create uncertainties $\gtrsim 0.5$ dex in the derived surface gravities ($\log g$). As a result, photometry alone is insufficient to determine the mass of a given WD with an accuracy better than $\approx 50\%$. Furthermore, without a precise mass (and therefore radius), τ_{cool} estimates must be based on T_{eff} alone and are uncertain by a factor of two or larger.

We therefore engaged in a campaign to obtain spectra for WDs in DWDs. Our targets included the new systems identified in Paper I, those photometrically selected from DR9, and WDs from pairs in the literature that lacked spectroscopy.⁹ Roughly 50 systems have $g \leq 19$ mag,

⁹ The Baxter et al. (2014) systems were published too recently to be included in our spectroscopic campaign, although as we discuss below several of these DWDs were also in our sample.

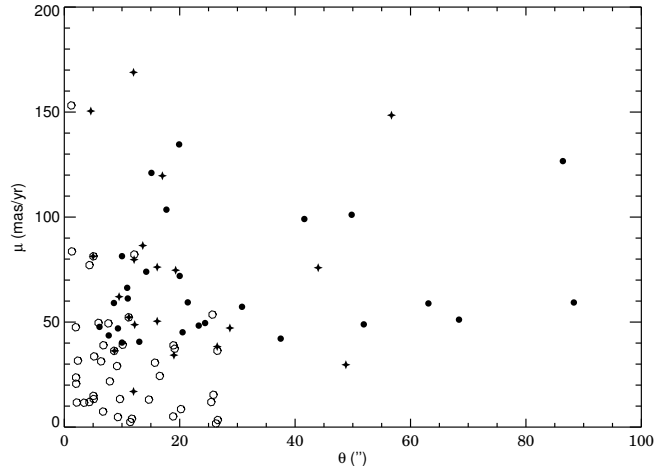


FIG. 7.— Total proper motion (μ) versus angular separation (θ) for candidate DWDs identified in our search for common proper motion pairs (filled circles), in Baxter et al. (2014, open circles), and in the literature (pluses). Although the Baxter et al. (2014) DWDs were also identified in SDSS, the overlap with our sample is small due to differences in the search techniques. Compared to other searches, we find systems with larger θ and μ .

making them ideal targets for the 3.5-m telescope at Apache Point Observatory (APO), NM.¹⁰

TABLE 1
DWDs IN THE DR9 FOOTPRINT NOT RECOVERED IN THIS SEARCH

System	Reason	$(u - g)$	$(g - r)$
LP 322-500A/B	A: low T_{eff}	0.97	0.35
LP 549-33/32	B: low T_{eff}	1.98	0.89
GD 322	B: low T_{eff}	0.81	0.35
LP 707-8/9	B: low T_{eff}	1.53	0.75
LP 701-69/70	B: low T_{eff}	2.26	0.98
LP 406-62/63	A: low T_{eff}	1.31	0.61
	B: low T_{eff}	1.72	0.83
LP 647-33/34	A: low T_{eff}	1.62	0.68
	B: low T_{eff}	1.65	0.76
LP 543-33/32	A: low T_{eff}	1.76	0.88
	B: low T_{eff}	2.08	1.07
LP 096-66/65	A: low T_{eff}	1.63	0.93
	B: low T_{eff}	1.13	0.53
LP 567-39/38	A: low T_{eff}	1.90	0.75
	B: low T_{eff}	0.96	0.48
G261-43	A: saturated		
J0926+1321	B: low μ^a		
GD 559	A,B: not stars ^b		

NOTE. — Objects with low T_{eff} have $(u - g)$ and $(g - r)$ colors outside our photometric selection region for WDs.

^a J0926+1321 was identified by Dobbie et al. (2012) as a wide DWD based on these authors' μ calculations.

^b The SDSS pipeline classified both stars as galaxies.

Over 13 half nights between 2012 Sep and 2013 Sep, we observed 34 pairs with the Dual Imaging Spectrograph in its high-resolution mode ($R \approx 2500$ at $H\beta$), which provides coverage from 3800 to 5000 Å on the blue CCD. The slit was rotated so that spectra were taken simultaneously of both candidate WDs in each pair. The spectra were therefore not obtained at the parallactic angle. Under ideal conditions, objects with separations as small as $2''$ could be distinguished for reduction.

¹⁰ The APO 3.5-m telescope is owned and operated by the Astrophysical Research Consortium.

TABLE 2
PROPERTIES OF CANDIDATE AND CONFIRMED WIDE DWDS

Name	α	δ	g (mag)	μ_α (mas yr $^{-1}$)	μ_δ (mas yr $^{-1}$)	θ (")	Targeted for Spectroscopy?	Source
J0000–0308	00:00:11.63	–03:08:31.9	20.11 \pm 0.02	42.43 \pm 3.25	–21.97 \pm 3.25	6.1	N	1
	00:00:12.04	–03:08:31.3	20.01 \pm 0.02	48.15 \pm 3.25	–21.02 \pm 3.25			
J0000–1051	00:00:22.53	–10:51:42.1	18.90 \pm 0.01	45.26 \pm 4.65	–23.81 \pm 4.65	16.1	N	2
	00:00:22.83	–10:51:26.6	20.21 \pm 0.02	42.37 \pm 4.08	–23.57 \pm 4.08			
CDDS1	00:01:42.84	+25:15:06.1	17.79 \pm 0.02			2.2	N	3
	00:01:42.79	+25:15:04.0	18.70 \pm 0.16					
J0002+0733	00:02:15.33	+07:33:59.1	17.85 \pm 0.01	–103.4 \pm 2.77	–64.37 \pm 2.77	15.1	Y	1
	00:02:16.13	+07:33:49.9	18.07 \pm 0.01	–103.62 \pm 2.85	–63.59 \pm 2.85			
J0029+0015	00:29:25.29	+00:15:59.8	19.59 \pm 0.01	–27.87 \pm 3.62	–23.24 \pm 3.62	8.7	N	2,3
	00:29:25.62	+00:15:52.7	18.46 \pm 0.01	–28.33 \pm 3.13	–22.58 \pm 3.13			
J0030+1810	00:30:51.75	+18:10:53.8	18.72 \pm 0.01			7.8	Y	1
	00:30:51.80	+18:10:46.1	18.73 \pm 0.01					
CDDS3	00:52:12.26	+13:53:02.0	17.71 \pm 0.03			6.8	N	3
	00:52:12.73	+13:53:01.1	18.89 \pm 0.03					
LP 406-62/63	01:04:56.33	+21:19:54.9	18.30 \pm 0.02	–210.33 \pm 2.51	–431.2 \pm 2.51	28.0	N	4
	01:04:57.81	+21:20:13.5	18.59 \pm 0.02	–209.48 \pm 2.62	–436.89 \pm 2.62			
J0105–0741	01:05:53.78	–07:41:22.2	20.51 \pm 0.03	–47.73 \pm 4.65	–66.24 \pm 4.65	10.0	N	1
	01:05:54.14	–07:41:30.8	18.57 \pm 0.01	–48.41 \pm 2.57	–61.63 \pm 2.57			
J0107+0511	01:07:17.20	+05:11:46.8	18.67 \pm 0.01	–59.61 \pm 2.86	–79.32 \pm 2.86	41.6	N	1
	01:07:19.89	+05:11:58.1	20.54 \pm 0.02	–49.86 \pm 3.48	–73.05 \pm 3.48			

REFERENCES. — 1: This work; 2: Paper I; 3: Baxter et al. (2014); 4: Literature (see Paper I for references).

NOTE. — The full table may be found in the online edition of the journal. The WDs in each pair are ordered by RA, regardless of the “A” or “B” designation that may exist in the literature.

All the spectra were trimmed, bias-corrected, cleaned of cosmic rays, flat-fielded, extracted, and dispersion-corrected using standard IRAF tasks.¹¹ The spectra were flux calibrated using bright WD spectrophotometric standards in the IRAF database. To improve the final signal-to-noise ratio (S/N), spectra were co-added using the IRAF routine `scombine`. Occasionally, the spectra to be combined were taken at different epochs, but the observing setup was identical across all observations.

Wide DWDS identified in Paper I, as well as a few WDs from our photometric search in DR9, have at least one SDSS spectrum ($R \approx 1800$), and we add these ≈ 30 SDSS spectra to our sample. Additionally, high-resolution Very Large Telescope (VLT; $R \approx 15,000$) spectra for ≈ 10 WDs from the Supernova Progenitor Survey (Koester et al. 2009) were provided by D. Koester (priv. communication). In total, we have 114 spectra for 97 WDs in wide DWDS; see Figure 8 for sample spectra. The contamination by non-WDs is extremely low: only one of the 97 objects for which we obtained spectra is not a WD (J2124–1620A is an A star).

3.2. Atmospheric Model Fits to Our Spectra

To obtain T_{eff} and $\log g$ for these WDs, we used the spectroscopic technique developed by Bergeron et al. (1992) and described in Gianninas et al. (2011, and references therein), which incorporates model atmospheres for WDs with $6.5 \leq \log g \leq 9.5$. The observed and theoretical spectra are normalized to a continuum set to unity, and the observed H β to H8 lines are fit simultaneously to the synthetic spectra (see Figure 9). The uncertainties in these quantities are a combination of the internal uncer-

¹¹ IRAF is distributed by the National Optical Astronomy Observatories, which are operated by the Association of Universities for Research in Astronomy, Inc., under cooperative agreement with the National Science Foundation.

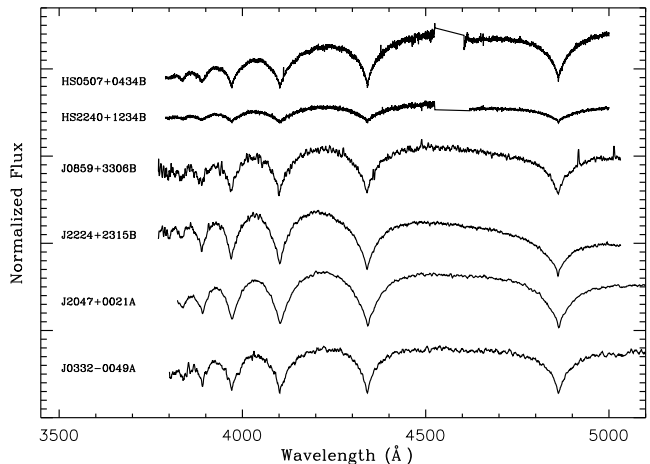


FIG. 8.— Sample VLT, APO, and SDSS WD spectra. These DAs have T_{eff} of 10,000–15,000 K. The top two spectra were taken with the VLT ($R \approx 14,000$) and are not flux calibrated. The middle two were taken at APO ($R \approx 2500$) and the bottom two by SDSS ($R \approx 1800$). These WDs range from $g \approx 16$ (HS 2240+1234B) to ≈ 19 mag (J0859+3306B). The spectra here and in Figure 24 have been smoothed using a boxcar average of width 5.

tainties, derived from the covariance matrix of the fitting functions, and external uncertainties of 1.2% in T_{eff} and 0.038 dex in $\log g$, derived from multiple observations of the same object (cf. Liebert et al. 2005).

These solutions are based on one-dimensional (1D) models using a standard mixing-length parameter $ML2/\alpha = 0.8$ (Tremblay et al. 2010). Tremblay et al. (2013) produced a new suite of WDs models and solved the radiation-hydrodynamics equations in three dimensions. These authors find that using this approach rather than mixing-length theory to approximate WDs with convective atmospheres leads to substantial differences in the derived masses for WDs with $7000 < T_{\text{eff}} < 12,000$ K. We applied the fitting formulas Tremblay et al. (2013) provide to the T_{eff} and $\log g$ solutions for all of the WDs in our sample. In the relevant region of parameter space, these adjustments tend to shift our WD solutions to lower

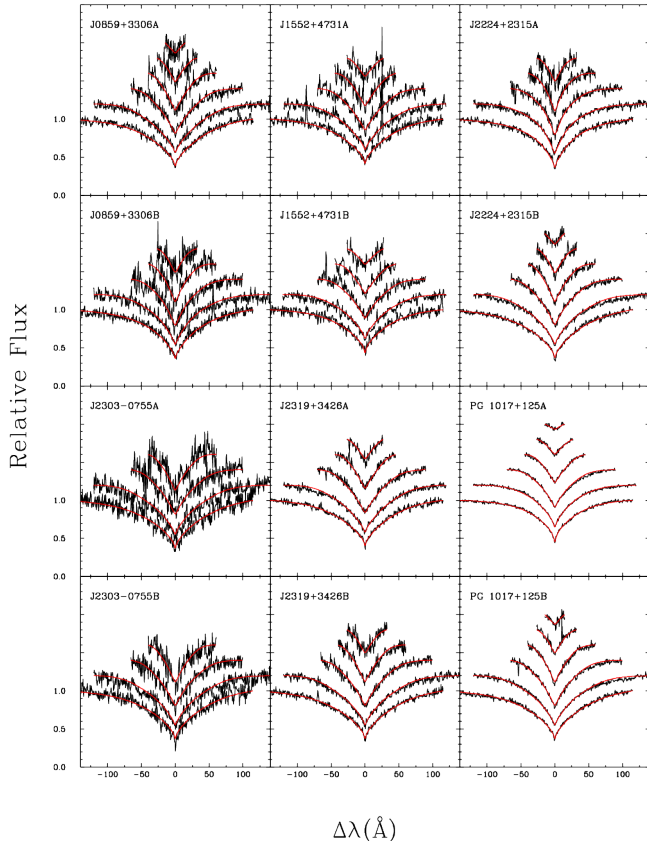


FIG. 9.— Our model fits (red) to the APO spectra of six DA/DA pairs. The number of Balmer lines fit ranges from four to six, starting with H β at the bottom. These fits are representative of the fits to all the WDs in our spectroscopic campaign.

T_{eff} and $\log g$ (or to older and less massive WDs) compared to mixing-length models.

Next, we used the Wood (1995) and Fontaine et al. (2001) models, depending on T_{eff} , to map our T_{eff} and $\log g$ values to τ_{cool} and masses (M_{WD}) for each of our WDs. Our fits also provide distances to the WDs which are determined by comparing photometric magnitudes with absolute magnitudes from the spectroscopic solutions. The resulting quantities for the DA+DA DWDs with spectra are given in Table 3.

3.3. Our Spectroscopic Sample

Our sample includes 27 DA/DA pairs. Table 3 shows that lower S/N spectra result in larger T_{eff} and $\log g$ uncertainties, and hence in the derived τ_{cool} and M_{WD} (for the dependence of these uncertainties on S/N, see figure 12, Gianninas et al. 2005). We therefore divided the sample into high-fidelity and low-fidelity pairs. We labeled systems with mass uncertainties $>0.1 M_{\odot}$ in at least one WD as low-fidelity. These pairs have spectra good enough to identify objects as DAs, but too poor to obtain accurate fits to model atmospheres.

As a further test, we considered the spectroscopic distances to each WD in these candidate DWDs. We designated systems with a distance difference $>25\%$ as low-fidelity. These distances do not necessarily identify these systems as random alignments, but instead reflect the accuracy of the spectral fits. After identifying eight sys-

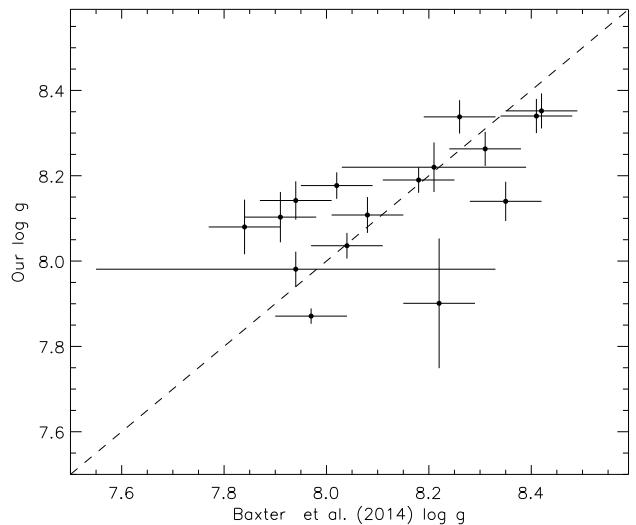
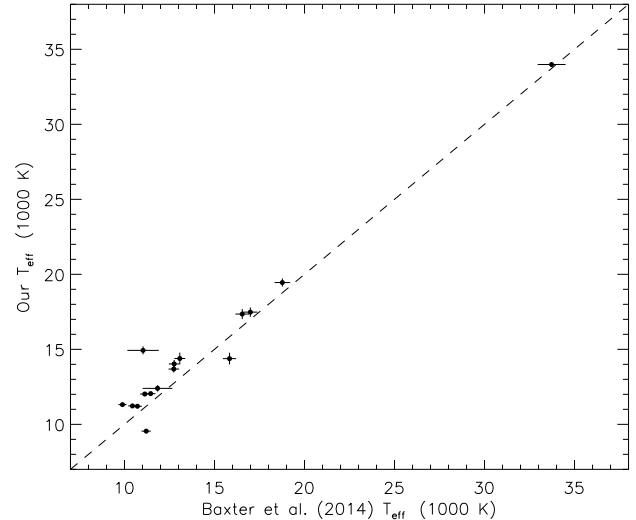


FIG. 10.— A comparison of T_{eff} and $\log g$ values derived by Baxter et al. (2014) with the values from our spectroscopic fits to the eight systems contained in both spectroscopic data sets. The dashed line shows the 1:1 correspondence. While the T_{eff} values are broadly consistent, our values appear to be slightly higher in most cases. By contrast, the $\log g$ values are well-matched for only half of the WDs and differ significantly for the other half, with no obvious trend in the differences.

tems as low-fidelity, we are left with 19 high-fidelity pairs as a starting point for our analysis below.

Our spectroscopic campaign also uncovered a number of pairs that, while interesting, cannot be used to constrain the IFMR. These include the detection of two systems containing a helium-atmosphere (DB) WD (one of which was already reported by Baxter et al. 2014). We also identify seven pairs that include a candidate magnetic (DAH) WD and six pairs with a (DC) WD too cool to show significant Balmer absorption features. Finally, we obtained spectra of the two known triple degenerate systems, G 21-15 and Gr 576/577, and identified PG 0901+140 as a candidate triple degenerate. These systems are discussed in greater detail in the Appendix.

TABLE 3
FIT RESULTS FOR THE DA/DA DWD SPECTROSCOPIC SAMPLE

Name	Telescope	# of Fitted Balmer Lines	S/N ^a	T_{eff} (K)	$\log g$	Distance (pc)	M_{WD} (M_{\odot})	τ_{cool} (Myr)
High-Fidelity Systems								
HS 0507+0434A	VLT	6	25,22	21450±310	8.00±0.04	51±2	0.629±0.024	50±7
HS 0507+0434B	VLT	6	19,12	12070±190	8.07±0.05	52±2	0.649±0.030	406±33
HS 2240+1234A	VLT	6	1,11	15320±230	8.04±0.04	96±3	0.636±0.026	197±17
HS 2240+1234B	VLT	5	1,10	14150±290	8.10±0.05	99±4	0.668±0.028	272±25
J0332-0049A	SDSS	6	25,23	10940±180	8.10±0.06	168±7	0.661±0.036	544±52
J0332-0049B	VLT	5	2,16	33990±490	7.87±0.05	177±6	0.594±0.022	6±<1
J0754+1239A	APO	5	17	14190±1070	8.24±0.12	258±23	0.755±0.074	335±95
J0754+1239B	APO	5	15	13690±630	8.31±0.11	247±22	0.801±0.072	415±91
J0827-0216A	APO	5	30	27310±450	8.49±0.06	260±13	0.933±0.035	68±11
J0827-0216B	APO	5	24	27860±490	8.58±0.07	265±16	0.989±0.039	79±14
J0859+3306A	APO	6	30	14930±340	7.98±0.06	232±10	0.602±0.034	194±23
J0859+3306B	APO	5	21	12140±280	8.18±0.07	228±12	0.718±0.045	470±59
J1231+5736A	APO	5	38	15360±290	8.01±0.05	217±18	0.618±0.031	185±19
J1231+5736B	APO	5	22	11190±230	7.92±0.08	231±13	0.556±0.046	404±47
J1257+1925A	SDSS	5	10	11750±470	7.91±0.16	456±51	0.552±0.089	350±83
J1257+1925B	SDSS	5	57	47800±990	7.76±0.07	503±32	0.579±0.029	2±<1
J1313+2030A	APO	5	30	14390±450	8.34±0.06	156±8	0.823±0.037	382±49
J1313+2030B	APO	6	40	14030±330	8.19±0.05	147±6	0.726±0.033	322±33
J1552+4731A	APO	5	24	17350±410	8.10±0.07	382±20	0.679±0.044	148±23
J1552+4731B	APO	5	27	19450±390	8.14±0.06	367±17	0.707±0.037	107±16
J2222-0828A	APO	5	41	14380±440	8.18±0.05	92±4	0.719±0.033	295±35
J2222-0828B	APO	5	29	11750±220	8.08±0.06	112±5	0.653±0.038	442±45
HS 2220+2146A	VLT	5	8,11	14270±270	8.15±0.04	79±2	0.702±0.022	289±22
HS 2220+2146B	VLT	5	10,16	18830±220	8.35±0.04	73±2	0.837±0.022	179±14
J2224+2315A	APO	5	39	10930±180	8.16±0.06	137±6	0.702±0.036	604±61
J2224+2315B	APO	6	47	13690±300	8.04±0.05	139±5	0.631±0.031	274±27
J2303-0755A	APO	5	15	14400±960	8.27±0.10	194±16	0.777±0.065	339±84
J2303-0755B	APO	5	18	13900±730	8.04±0.09	223±15	0.635±0.054	264±54
J2319+3426A	APO	5	43	16320±270	8.12±0.05	162±6	0.684±0.030	183±18
J2319+3426B	APO	5	33	14140±450	8.05±0.05	172±7	0.641±0.032	255±31
LP 128-254	APO	6	35	14030±470	8.07±0.06	164±7	0.652±0.034	269±34
LP 128-255	SDSS	5	25	11080±200	7.98±0.07	164±8	0.589±0.040	447±45
LP 370-50	APO	5	30	7560±120	8.19±0.09	59±4	0.710±0.055	1668±324
LP 370-51	APO	5	31	7210±120	8.14±0.10	61±4	0.681±0.061	1723±349
PG 0901+140A ^b	APO	6	67	9100±140	7.78±0.08	59±3	0.474±0.041	585±57
PG 0901+140B	APO	6	39	8120±120	7.89±0.07	58±3	0.531±0.039	886±87
PG 0922+162A	VLT	5	15,15	24480±350	8.28±0.04	158±6	0.797±0.028	59±9
PG 0922+162B	VLT	4	20,8	26500±440	9.04±0.06	110±7	1.220±0.023	227±23
PG 1017+125A	APO	6	90	22130±330	7.99±0.04	106±4	0.622±0.024	41±6
PG 1017+125B	APO	6	50	13580±240	8.12±0.05	108±4	0.681±0.030	317±28
Low-Fidelity Systems								
J11002+3606A	APO	5	20	9720±160	8.42±0.10	152±12	0.863±0.063	1287±296
J11002+3606B	SDSS	4	9	11650±580	8.26±0.21	226±38	0.767±0.135	594±217
J1110+4517A	APO	6	23	13700±370	8.10±0.06	113±5	0.670±0.038	301±36
J1110+4517B	APO	5	46	19000±300	8.12±0.05	152±6	0.692±0.029	111±13
J1203+4948A	APO	6	25	11410±220	8.12±0.07	119±6	0.674±0.041	502±56
J1203+4948B	APO	5	14	7250±150	8.06±0.21	118±18	0.631±0.129	1507±621
J1309+5503A	SDSS	5	13	8120±160	7.94±0.18	136±16	0.560±0.100	951±234
J1309+5503B	SDSS	5	22	8090±140	8.17±0.11	85±7	0.698±0.071	1345±277
J1546+6159A	APO	5	20	10880±190	7.84±0.07	244±12	0.514±0.039	398±39
J1546+6159B	APO	6	70	16510±270	8.06±0.05	143±6	0.649±0.029	159±16
J1703+3304A ^c	SDSS	5	12	9400±180	7.63±0.16	239±24	0.424±0.069	874±72
J1703+3304B	SDSS	6	33	11030±190	8.19±0.06	156±7	0.718±0.037	614±64
J0030+1810A	APO	5	11	14070±1050	8.42±0.18	222±33	0.870±0.115	458±167
J0030+1810B	APO	5	5	15620±2930	8.43±0.35	244±77	0.880±0.214	351±306
J1113+3238A	SDSS	4	10	6680±230	7.33±0.54	156±49	0.307±0.185	1474±466
J1113+3238B	SDSS	4	8	7760±260	8.82±0.33	78±27	1.107±0.170	3646±233
J2326-0023A	SDSS	4	9,9	7530±180	8.45±0.23	114±21	0.884±0.151	3028±968
J2326-0023B	SDSS	6	28	10530±170	8.02±0.06	124±5	0.611±0.036	538±50

NOTE. — When multiple spectra were available, we list the fit to the DA’s best spectrum, which we define as the fit that produces a distance that best matches its companion’s. For previously identified systems, we label the WDs “A” and “B” as in the literature. We order newly identified systems by their RA as opposed to e.g., their relative brightnesses.

^a Entries with more than one listed S/N indicate that multiple spectra were used to fit for the WD parameters.

^b Given its anomalously low mass, PG 0901+140A may be an unresolved triple system.

^c Despite its low mass, J1703+3304A (CDDS40-B) is unlikely to be an unresolved double degenerate (cf. discussion in the Appendix), because the discrepant distances indicate a poor fit.

3.4. Comparison to the Baxter et al. (2014) Fit Results

Baxter et al. (2014) identified 53 DWDs, and 12 are included in our spectroscopic sample. Baxter et al. (2014) obtained spectra for eight of these pairs. In Figure 10, we compare the $\log g$ and T_{eff} values these authors derived to ours. Half the WDs have T_{eff} and $\log g$ values in agreement; the other half have significantly different spectroscopic solutions, particularly in $\log g$. This is similar to what Baxter et al. (2014) found when comparing their spectroscopic results to the SDSS-derived results of Kleinman et al. (2013): of the five Kleinman et al. (2013) WDs for which Baxter et al. (2014) have spectra, two have significantly differing $\log g$ values.

We show the WD masses derived from these spectral solutions for the 16 WDs in both spectroscopic samples in Figure 11. We find that our M_{WD} estimates are systematically larger by $\approx 0.05 M_{\odot}$. We ascribe these differences to the combination of observations made with instruments with different resolutions and of spectral fitting done with different techniques and atmospheric models.

As the Baxter et al. (2014) spectroscopic sample represents a significant addition to our own, we include the WDs in our analysis below. For systems in both the Baxter et al. (2014) spectroscopic sample and our own, we use the values derived from our spectra.

3.5. Our DWD Sample for Constraining the IFMR

Standard stellar evolution theory predicts that the more massive WDs in DWDs are also the older WDs: more massive stars evolve faster, becoming more massive WDs with larger τ_{cool} than their less massive companions. Of the 20 high-fidelity systems in Table 3, PG 0901+140 may be a triple system (see discussion in the Appendix) and five appear to host a more massive WD that is younger than its companion: J1231+5736, J1552+4731 (CDDS36), J2222-0828 (CDDS48), HS 2220+2146, and LP 128-254/255. We remove these and use the remaining 14 systems for our analysis.

We then consider the 10 Baxter et al. (2014) systems for which we have poor or no spectroscopic data. We remove five of these systems from our analysis. One of the WDs in CDDS16 has poor S/N; the higher-order Balmer lines are particularly noisy, which impacts the determination of $\log g$. Baxter et al. (2014) identified CDDS30 as a possible triple system. CDDS31 has a projected separation of ≈ 100 AU and could therefore have had previous mass-transfer episodes. The more massive WD in CDDS26 appears to be younger than its companion. Finally, SDSS spectra are available for both WDs in CDDS7, but the spectra are very poor. We add the remaining five pairs to our sample, so that we now have 19 DWDs with which to constrain the IFMR (see Table 4).

4. CONSTRAINING THE IFMR WITH DWDs

We begin by examining several of the basic assumptions that allow one to use DWDs to constrain the IFMR. These are that the two WDs are co-eval and have not been subjected to significant mass transfer during their lifetimes, that our DWD progenitors did not vary significantly in metallicity, and that the pre-WD lifetimes produced by stellar evolution codes for stars of a given mass are relatively insensitive to the parameters one uses in these calculations. We then revisit

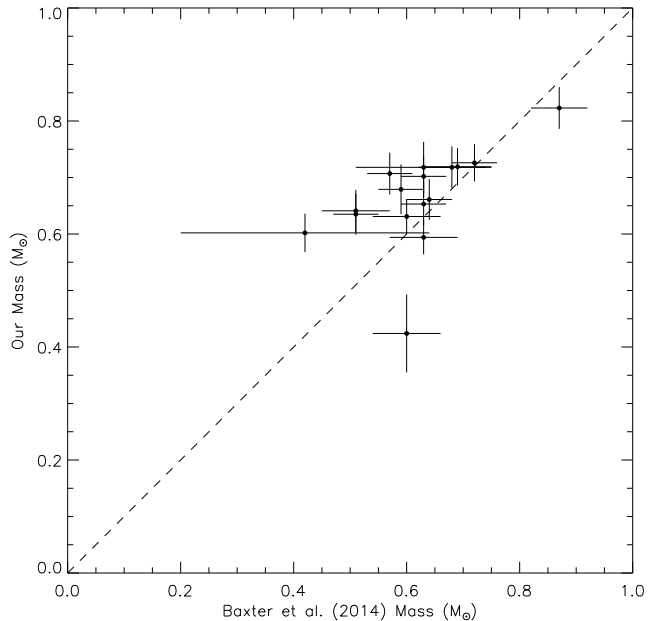


FIG. 11.— Comparison of the M_{WD} of Baxter et al. (2014) and obtained from our spectra for 16 WDs in eight DWDs included in both spectroscopic samples. The dashed line shows the 1:1 correspondence. Our M_{WD} estimates are systematically larger by $\approx 0.05 M_{\odot}$, presumably due to the use of spectra with different resolutions and fitting codes with different model atmospheres.

the Finley & Koester (1997) result before developing a flexible, Bayesian method that takes into account measurement uncertainties and provides statistically rigorous constraints on the IFMR.

4.1. Examining the Underlying Assumptions

4.1.1. Co-evolution and Independence of Wide DWDs

Binary star formation theory suggests that the collapse of gas clouds in multistellar systems occurs on a dynamical timescale (Shu et al. 1987); for typical binaries, this is < 1 Myr. This expectation has been borne out by observations of binaries in the Taurus-Auriga cluster by Kraus & Hillenbrand (2009), which suggest that the age difference of the stars in binaries is even smaller than that of stars within an open cluster. Since the probability that field DWD progenitor systems formed through gravitational capture is extraordinarily small, we can safely assume the stars in a wide binary are born together through fragmentation (Boss 1988).

Wide binaries with small enough separations could have interacted in the past, potentially through wind-fed mass transfer. Indeed, below some critical (but still relatively large) separation, some amount of mass transfer is unavoidable, and may impact the system's evolution. For example, Mira, with a separation of ≈ 70 AU, shows mass accretion at a rate of $\approx 10^{-10} M_{\odot} \text{ yr}^{-1}$ (Sokoloski & Bildsten 2010), high enough to potentially induce periodic nova eruptions on the WD surface every $\approx \text{Myr}$, which would affect its derived τ_{cool} .

Such mass accretion could be due to so-called wind Roche lobe overflow (Mohamed & Podsiadlowski 2007, 2012). These authors argue that when an AGB donor is

TABLE 4
 DA/DA DWDs USED TO CONSTRAIN THE IFMR

Name	$M_{\text{WD},1}$ (M_{\odot})	$M_{\text{WD},2}$ (M_{\odot})	$\tau_{\text{cool},1}$ (Myr)	$\tau_{\text{cool},2}$ (Myr)	Distance ^a (pc)	θ (asec)	s (AU)
HS 0507+0434	0.649±0.030	0.629±0.024	406±33	50±7	51	18	919
HS 2240+1234	0.668±0.028	0.636±0.026	272±25	197±17	97	12	1166
J0332−0049	0.661±0.036	0.594±0.022	544±52	6±< 1	173	19	3290
J0754+1239	0.801±0.072	0.755±0.074	415±91	335±95	252	2	504
J0827−0216	0.989±0.039	0.933±0.035	79±14	68±11	262	3	787
J0859+3306	0.718±0.045	0.602±0.034	470±59	194±23	231	9	2080
J1257+1925	0.579±0.029	0.552±0.089	2±< 1	350±83	490	12	5888
J1313+2030	0.823±0.037	0.726±0.033	382±49	322±33	150	6	901
J2224+2315	0.702±0.036	0.631±0.031	604±61	274±27	138	3	415
J2303−0755	0.777±0.065	0.635±0.054	339±84	264±54	209	8	1670
J2319+3426	0.684±0.030	0.641±0.032	183±18	255±31	167	5	836
LP 370-50/51	0.710±0.055	0.681±0.061	1670±320	1720±350	60	13	781
PG 0922+162	1.220±0.023	0.797±0.028	227±23	59±9	158	5	791
PG 1017+125	0.681±0.030	0.622±0.024	317±28	41±6	107	49	5250
CDDS3	0.592±0.036	0.579±0.034	78±14	491±63	256	7	1792
CDDS6	0.668±0.039	0.655±0.040	31±8	114±19	192	2	385
CDDS9	0.598±0.058	0.535±0.070	142±32	376±69	506	12	6080
CDDS14	0.644±0.041	0.590±0.045	428±54	598±91	211	5	1056
CDDS40	0.694±0.043	0.634±0.040	876±129	530±70	187	11	1419

NOTE. — In this table WDs 1 and 2 are the more and less massive WDs in the pair, respectively.

^a This is the average of the distance to each WD.

emitting a slow wind, a companion at tens of AU can channel a substantial fraction of the lost mass. Abate et al. (2013) suggest that wind Roche lobe overflow can occur when the companion is at a separation less than the AGB’s dust formation radius, because at larger separations the increased opacity due to dust means that radiation pressure will quickly push the wind to escape the system. Observations suggest that this radius is also \approx tens of AU (Höfner 2009; Karovicova et al. 2013).

More work is needed to determine the spatial separation at which the effects of wind-fed mass transfer can be ignored. However, since the smallest projected binary separation of the wide DWDs in our sample is hundreds of AU (see Table 4), we expect mass accretion to be negligible, even in prior evolutionary states when the binaries may have had somewhat smaller separations.

4.1.2. Metallicity of the DWD progenitors

In their analysis of WDs in the open cluster M37, Kalirai et al. (2005) found that their data were consistent with stars of a given M_i producing higher mass WDs than in previous studies. These authors suggested that the lower metallicity of M37 might result in less mass loss on the AGB and, therefore, more massive WDs.

Theory supports this interpretation: Renedo et al. (2010) found that metal-poor stars undergo more thermal pulses on the AGB, resulting in more massive WDs. Variations in metallicity should result in WD masses varying by $\approx 0.1 M_{\odot}$ for a given M_i . However, for near-solar metallicities, the IFMR does not vary much (Marigo & Girardi 2007; Meng et al. 2008; Romero et al. 2015).

Fortunately, the WDs in our sample should have roughly similar, near-solar metallicities. We cannot directly test for the metallicity of a WD progenitor, but there are indications that most disk stars born in the past several Gyr likely have similar metallicities. For example, in a study of local F and G type stars, Fuhrmann (1998) found that kinematically identified thin-disk stars have [Fe/H] and [Mg/H] metallicity indicators within 0.3

dex of solar.

As shown in Figure 2, our subset of candidate WDs with measured proper motions almost all have transverse velocities consistent with being in the Galactic disk. Furthermore, since we selected relatively hot WDs for the spectroscopic follow-up described in Section 3, all of the wide DWDs in our sample are relatively young. We therefore expect the progenitors of the WDs in our sample to have had a metallicity close to $z = 0.02$.

4.1.3. Robustness of the Pre-WD Lifetime Function

We obtain a pre-WD lifetime function, \mathbf{F} , by running models from MESA. MESA is a suite of modules that includes integrated equations-of-state tables, opacity tables, nuclear reaction networks, and elemental diffusion rates. The stellar evolution module, MESA `star`, solves the stellar structure equations using a 1D, adaptive Lagrangian algorithm. Built with state-of-the-art prescriptions, MESA `star` has been extensively tested and compared to observations and other stellar evolution codes (Paxton et al. 2011, 2013, 2015).

 TABLE 5
 MESA MODEL PARAMETERS

Parameter	Fiducial Model
number of isotopes	26 (up to Mg)
metallicity	$z = 0.02$
mixing length	$\alpha_{\text{MLT}} = 1.73$
overshoot parameter	$f = 0.014$
photospheric model	<code>simple_photosphere</code>
RGB mass loss	Reimers, $\eta = 0.5$
AGB mass loss	Blocker, $\eta = 0.5$
opacity tables	Grevesse & Noels (1993)
convection	Schwartzchild criterion
rotation	off

The parameters and prescriptions used in our fiducial model are given in Table 5. Stars begin as gas clouds on the pre-main-sequence. Once fusion begins, the reaction network tracks the concentrations of isotopes. Convection is treated as an exponential diffusive process, with

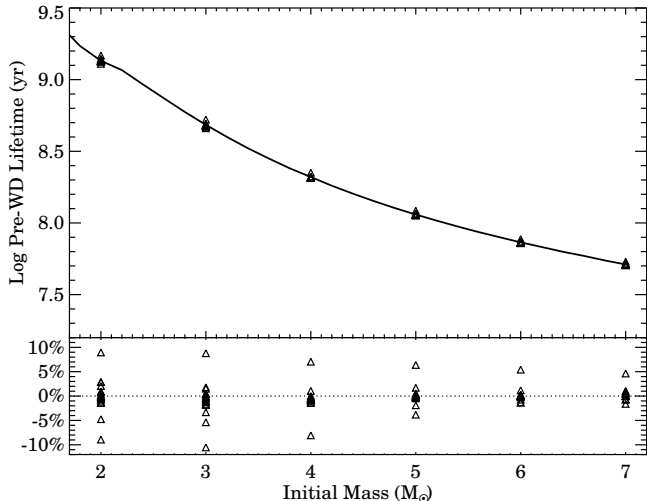


FIG. 12.— Pre-WD lifetime (approximated by the age at the 1TP) as a function of initial mass. The solid line shows ages produced by our fiducial model, while the triangles show the results of MESA models generated varying a number of prescriptions. The lower panel shows that the pre-WD lifetimes produced by these tests are robust, as they typically vary by less than 5% even for very different models.

a diffusive constant and adjustable scale length based on the pressure scale height; semi-convection is not included in our fiducial model. Exponential mixing near the convective boundary due to overshooting is included (Freytag et al. 1996; Herwig et al. 1997).

We stop our model at the first thermal pulse (1TP), the start of the thermally pulsing AGB (TP-AGB). We set the star’s age here as its pre-WD lifetime, as evolution through the TP-AGB is quick (10^5 to 10^6 yr, or $<1\%$ of its lifetime), with higher mass stars evolving faster (Vassiliadis & Wood 1993).

We run simulations for our fiducial model for $M_i = 0.6$ – $8.0 M_{\odot}$ in $0.2 M_{\odot}$ steps. To determine the pre-WD lifetime for an arbitrary M_i , we linearly interpolate over the values in this grid. The resulting pre-WD lifetime function is indicated by the solid line in Figure 12.

In comparing MESA to other stellar evolution codes, Paxton et al. (2011) found that the derived stellar lifetimes agreed within $\approx 5\%$. However, Paxton et al. (2013) showed that the choice of parameters and prescriptions may have a stronger impact on the stellar lifetime. We therefore tested 19 MESA models in addition to our fiducial model, varying the metallicity, atmospheric models, opacity tables, mixing length, and also included rotation and semi-convection. A detailed discussion of how each parameter affects the stellar lifetime is outside the scope of this work; we used these models to gauge the level of uncertainty in the stellar lifetimes.

The symbols in Figure 12 show how the lifetimes we obtain vary from model to model for $2 \leq M_i \leq 7 M_{\odot}$. The bottom panel shows that the majority of our 19 models produce lifetimes within a few percent of those obtained using our fiducial model. The largest differences in the lifetimes occur when changing the opacity tables (which are calculated based on different elemental abundances) and metallicities. Models run with the Asplund et al. (2009) opacity tables lead to lifetimes longer by $\approx 10\%$ than those from models run with the fiducial Grevesse &

Noels (1993) tables. Conversely, models with sub-solar metallicities lead to shorter lifetimes (e.g., by $\approx 10\%$ for $z = 0.01$). In principle, these stellar evolution uncertainties should be included in a comprehensive model. However, as they are relatively minor and since we expect our DWD progenitors to have had similar, approximately solar metallicities, we ignore these uncertainties in our analysis below.

4.2. Revisiting the Finley & Koester (1997) Result

Finley & Koester (1997) constrained the IFMR using the wide DWD PG 0922+162. These authors compared the more massive WD ($\gtrsim 1.10 M_{\odot}$) to similarly massive WDs in open clusters for which M_i had been published, thereby obtaining $M_i = 6.5 \pm 1.0 M_{\odot}$ for this WD.¹² Finley & Koester (1997) converted this mass into a pre-WD lifetime of 42–86 Myr, to which they added the τ_{cool} of the massive WD to derive a system age of 320 ± 32 Myr. These authors then used the less massive WD in PG 0922+162 ($M_{\text{WD}} = 0.8 M_{\odot}$) to constrain the IFMR: they derived a pre-WD lifetime for this WD of 231 ± 34 Myr by subtracting its τ_{cool} from the system age and obtained $M_i = 3.8 \pm 0.2 M_{\odot}$ for its progenitor.

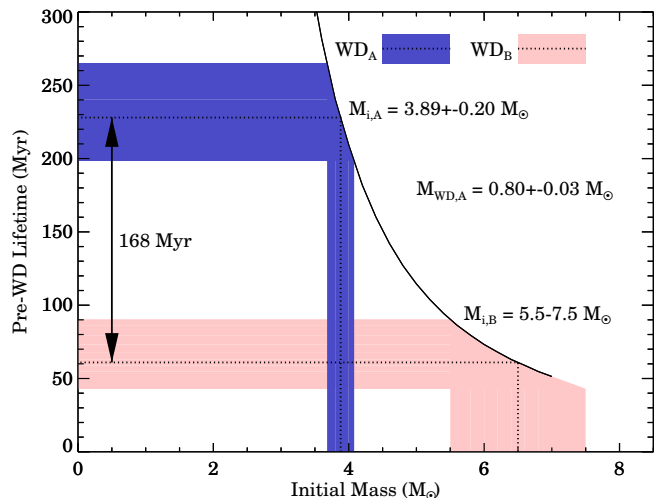


FIG. 13.— Converting M_i into pre-WD lifetimes. Finley & Koester (1997) assigned the more massive WD_B in PG 0922+162 a $M_i = 6.5 \pm 1.0 M_{\odot}$, which corresponds to a pre-WD lifetime of 43–90 Myr (we use our mesa stellar lifetime function here). Adding the τ_{cool} difference between the two WDs gives a pre-WD lifetime of 198–265 Myr for the less massive WD_A. We derive a corresponding $M_i = 3.89 \pm 0.20 M_{\odot}$ for WD_A; Finley & Koester (1997) found $3.8 \pm 0.2 M_{\odot}$. Despite the relatively large uncertainty in the initial mass of WD_B, the uncertainty in the initial mass of WD_A is small, particularly compared to typical uncertainties derived from other observational methods.

In Figure 13 we reproduce one of the key steps in this analysis, the conversion of pre-WD lifetimes into initial masses. Because the relation between lifetime and mass is steeper for longer-lived, lower-mass stars, even relatively large uncertainties in the assumed M_i for the more massive WD in PG 0922+162 results in stringent constraints on the M_i of the less massive WD. Indeed, the

¹² This is one of the difficulties in directly applying this method to other DWDs, since comparing the more massive WD in a DWD to WDs in open clusters cannot always be done for a generic DWD.

Finley & Koester (1997) result is one of the most stringent constraints on the IFMR, and is one of the reasons why Weidemann (2000) anchored his semi-empirical IFMR at $M_i = 4 M_\odot$ and $M_{\text{WD}} = 0.8 M_\odot$.

4.3. A New Parametric Model for the IFMR

While the Finley & Koester (1997) result indicates that DWDs can be powerful systems for constraining the IFMR, these authors' approach cannot be replicated for a generic set of wide DWDs such as the one we have assembled. We therefore develop a new method for constraining the IFMR with wide DWDs by constructing a parametric model for the IFMR. Our approach is presented in schematic form in Figure 14.

We begin by considering the observables: the cooling ages, $\tau_{\text{cool},1}$ and $\tau_{\text{cool},2}$, and WD masses, $M_{\text{WD},1}$ and $M_{\text{WD},2}$. If the WDs are indeed co-eval and evolved independently, the difference in the cooling ages must be equal to the difference in the pre-WD lifetimes, τ_1 and τ_2 . If WD₁ is the more massive, older WD and therefore had the shorter pre-WD lifetime,

$$\Delta\tau_{\text{cool}} = -\Delta\tau \quad (1)$$

$$\tau_{\text{cool},1} - \tau_{\text{cool},2} = -(\tau_1 - \tau_2). \quad (2)$$

While $\tau_{\text{cool},1}$ and $\tau_{\text{cool},2}$ are observed, τ_1 and τ_2 are obtained by a functional transformation from M_{WD} :

$$\tau = \mathbf{F}M_i \quad (3)$$

$$= \mathbf{F}\mathbf{G}^{-1}M_{\text{WD}} \quad (4)$$

where \mathbf{F} is the pre-WD lifetime function, and we have applied the inverse IFMR, \mathbf{G}^{-1} to obtain M_i from the observed WD masses. Combining these, we obtain:

$$\tau_{\text{cool},1} - \tau_{\text{cool},2} = \mathbf{F}\mathbf{G}^{-1}M_{\text{WD},2} - \mathbf{F}\mathbf{G}^{-1}M_{\text{WD},1}. \quad (5)$$

Since $\mathbf{F}M_i$ can be determined with accuracy from stellar evolution codes (see Section 4.1.3), we now need to find the best \mathbf{G}^{-1} that satisfies Equation 5. Below, we construct a likelihood function that evaluates the ability for any \mathbf{G}^{-1} to account for the observations. We then define a parametric model for \mathbf{G} , and iterate over these model parameters, Θ , to find the highest likelihood set. As discussed below, because of the functional form of the IFMR, finding the best \mathbf{G}^{-1} is directly equivalent to finding the best \mathbf{G} and therefore constraining the IFMR.

4.3.1. Bayesian Framework

We calculate a likelihood function for a particular IFMR, using a Bayesian hierarchical model to account for measurement uncertainties. We begin with Bayes' rule:

$$P(\Theta | \mathbf{D}, I) = \frac{P(\mathbf{D} | \Theta, I)P(\Theta | I)}{P(\mathbf{D} | I)}, \quad (6)$$

where \mathbf{D} is the set of observed wide DWDs,¹³ and I represents our prior information and assumptions about the data and model. For instance, observational uncertainties are contained within I . $P(\Theta | \mathbf{D}, I)$ is the posterior probability we are looking for, $P(\mathbf{D} | I)$ is a constant dependent only on the data, $P(\Theta | I)$ are the priors on our

¹³ \mathbf{D} refers to the set of wide DWDs, while D refers to an individual system.

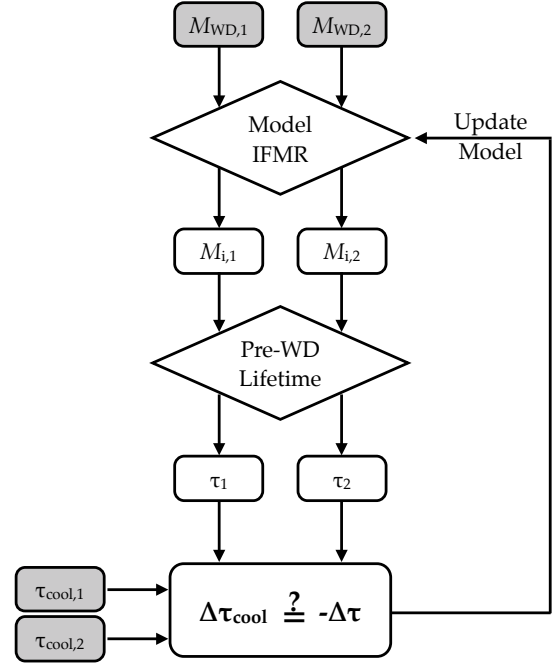


FIG. 14.— A schematic summary of our method. Gray boxes indicate observed quantities. We convert each M_{WD} into a M_i using a candidate IFMR, and then find the corresponding pre-WD lifetime, τ , using the function shown in Figure 12. The difference of these lifetimes should be equal to $\Delta\tau_{\text{cool}}$, which we obtain from the two observed τ_{cool} . Our problem is then reduced to iterating over our model parameters to find the IFMR that makes this equality true for our set of wide DWDs.

model, and $P(\mathbf{D} | \Theta, I)$ is the likelihood. The posterior probability over the set of data is a product over individual measurements:

$$P(\mathbf{D} | \Theta, I) = \prod_{D \in \mathbf{D}} P(D | \Theta, I). \quad (7)$$

We now substitute in the individual observables:

$$P(D | \Theta, I) = P(M'_1, M'_2, \Delta\tau_{\text{cool}}' | \Theta, I). \quad (8)$$

To construct our likelihood function, we first marginalize over τ_1 , τ_2 , and $\Delta\tau$:

$$P(D | \Theta, I) = \int_0^\infty \int_0^\infty \int_{-\infty}^\infty d\tau_1 d\tau_2 d\Delta\tau \\ \times P(\tau_1, \tau_2, \Delta\tau, M'_1, M'_2, \Delta\tau_{\text{cool}}' | \Theta, I) \quad (9)$$

Hereafter, primed quantities refer to observed values and unprimed quantities refer to true values. Because observations of each WD and of $\Delta\tau_{\text{cool}}$ are all independent, we can factor this probability:

$$P(D | \Theta, I) = \int_0^\infty \int_0^\infty d\tau_1 d\tau_2 P(M'_1 | \tau_1, \Theta, \sigma_{M_1}) \\ \times P(M'_2 | \tau_2, \Theta, \sigma_{M_2}) P(\tau_1 | \Theta) P(\tau_2 | \Theta) \\ \times \int_{-\infty}^\infty d\Delta\tau P(\Delta\tau_{\text{cool}}' | \Delta\tau, \sigma_{\Delta\tau_{\text{cool}}}) \\ \times P(\Delta\tau | \tau_1, \tau_2), \quad (10)$$

where here we also factored I into individual observational uncertainties. The conditional probability over $\Delta\tau$

is a delta function:

$$P(\Delta\tau | \tau_1, \tau_2) = \delta(\Delta\tau - \tau_1 + \tau_2), \quad (11)$$

and the conditional probability over $\Delta\tau_{\text{cool}'}$ is a Gaussian distribution:

$$P(\Delta\tau_{\text{cool}' | \Delta\tau, \sigma_{\Delta\tau_{\text{cool}'}}}) = \mathcal{N}(-\Delta\tau | \Delta\tau_{\text{cool}'}, \sigma_{\Delta\tau_{\text{cool}'}}), \quad (12)$$

where the negative sign is from Equation 1. After reducing the innermost integral, Equation 10 simplifies to:

$$P(D | \Theta, I) = \int_0^\infty \int_0^\infty d\tau_1 d\tau_2 P(M'_1 | \tau_1, \Theta, \sigma_{M_1}) \times P(M'_2 | \tau_2, \Theta, \sigma_{M_2}) P(\tau_1 | \Theta) P(\tau_2 | \Theta) \times \mathcal{N}[(\tau_1 - \tau_2) | \Delta\tau_{\text{cool}'}, \sigma_{\Delta\tau_{\text{cool}'}}]. \quad (13)$$

Evaluating Equation 13 is unnecessarily computationally expensive, since only a small region of the domain has any contributing probability. We therefore use a Monte Carlo method to approximate the double integral as a single sum over randomly drawn τ_1 and τ_2 . We make this approximation with a single rather than double sum because the first two terms in the integrand, the observed WD masses, are independent of each other:

$$P(D | \Theta, I) \approx \frac{1}{N} \sum_k P(\tau_{1k} | \Theta) P(\tau_{2k} | \Theta) \times \mathcal{N}[(\tau_{1k} - \tau_{2k}) | \Delta\tau_{\text{cool}'}, \sigma_{\Delta\tau_{\text{cool}'}}], \quad (14)$$

where there are N random draws of τ_{1k} and τ_{2k} from the distributions:

$$\begin{aligned} \tau_{1k} &\sim P(\tau_1 | M'_1, \Theta, \sigma_{M_1}) = P(M'_1 | \tau_1, \Theta, \sigma_{M_1}) \\ \tau_{2k} &\sim P(\tau_2 | M'_2, \Theta, \sigma_{M_2}) = P(M'_2 | \tau_2, \Theta, \sigma_{M_2}). \end{aligned} \quad (15)$$

Here, we have applied Bayes' theorem to make the equalities on the right side of these equations. To generate these random distributions:

$$\begin{aligned} P(\tau_1 | M'_1, \Theta, \sigma_{M_1}) &= P(\mathbf{GF}^{-1}\tau_1 | M'_1, \sigma_{M_1}) \left| \frac{d\mathbf{GF}^{-1}\tau_1}{d\tau_1} \right| \\ P(\tau_2 | M'_2, \Theta, \sigma_{M_2}) &= P(\mathbf{GF}^{-1}\tau_2 | M'_2, \sigma_{M_2}) \left| \frac{d\mathbf{GF}^{-1}\tau_2}{d\tau_2} \right|. \end{aligned} \quad (16)$$

We determine the derivatives numerically, and the observational uncertainties in WD mass are Gaussian:

$$\begin{aligned} P(\mathbf{GF}^{-1}\tau_1 | M'_1, \sigma_{M_1}) &= \mathcal{N}(\mathbf{GF}^{-1}\tau_1 | M'_1, \sigma_{M_1}) \\ P(\mathbf{GF}^{-1}\tau_2 | M'_2, \sigma_{M_2}) &= \mathcal{N}(\mathbf{GF}^{-1}\tau_2 | M'_2, \sigma_{M_2}). \end{aligned} \quad (17)$$

Equations 7, 14, 16, and 17 define the model likelihood. For a given model, finding the model parameters, Θ , implied by our set of wide DWDs involves maximizing the likelihood function in Equation 14.

We are interested in determining the precision of the constraints we can place on our model parameters, and therefore chose a Monte Carlo technique rather than a maximum-likelihood calculation. Specifically, we used the Markov Chain Monte Carlo algorithm `emcee` (Foreman-Mackey et al. 2013), which implements an affine invariant, ensemble sampler algorithm to search the parameter space (Goodman & Weare 2010).

4.3.2. Parametric Model

We define our model by first including a parametrization that determines $P(\tau_1 | \Theta)$ and the corresponding

quantity for the second WD. To keep the dimensionality of the problem low, our likelihood function (Equation 14) marginalizes over all possible pre-WD lifetimes.

Standard stellar evolution precludes the existence of WDs more massive than the Chandrasekhar mass ($\approx 1.35 M_\odot$). At the other end, the Galaxy is not old enough to produce isolated WDs less massive than $\lesssim 0.45 M_\odot$ (Kilic et al. 2007), except in cases of extremely high metallicity. We therefore use a truncated Gaussian to describe the WD mass distribution, $0.45 M_\odot < M_{\text{WD}} < 1.35 M_\odot$, which we can model using the mean mass μ_{WD} and standard deviation $\sigma_{M_{\text{WD}}}$ as parameters.

We set flat priors on μ_{WD} and $\sigma_{M_{\text{WD}}}$, limiting their ranges:

$$\begin{aligned} \frac{\mu_{\text{WD}}}{M_\odot} &\in [0.1, 1.5] \\ \frac{\sigma_{\text{WD}}}{M_\odot} &\in [0.1, 1.0]. \end{aligned} \quad (18)$$

More complex models may better represent the WD mass distribution, but for our purposes, this Gaussian model is sufficient. This allows us to add to our model two hyperparameters that weigh τ_1 and τ_2 :

$$P(\tau_1 | \Theta) = \mathcal{N}(\mathbf{GF}^{-1}\tau_1 | \mu_{\text{WD}}, \sigma_{M_{\text{WD}}}) \quad (19)$$

$$P(\tau_2 | \Theta) = \mathcal{N}(\mathbf{GF}^{-1}\tau_2 | \mu_{\text{WD}}, \sigma_{M_{\text{WD}}}). \quad (20)$$

Next, we choose a parametric form for the IFMR, \mathbf{G} . Observational IFMR constraints (such as those from open clusters) are traditionally fit with a linear relation (e.g., Williams et al. 2009). Here we opt for a more complex model based on our expectation that the IFMR has three distinct regimes: for $M_i \lesssim 2 M_\odot$, stars undergo a degenerate helium flash (Sweigart & Gross 1978). For $2 \lesssim M_i \lesssim 4 M_\odot$, stars will undergo stable, non-degenerate helium burning. Finally, second dredge-up becomes important for stars with $M_i \gtrsim 4 M_\odot$ (Dominguez et al. 1999).

Theoretical IFMRs from stellar evolution codes indicate roughly linear IFMRs for each of these regimes, with pivots at $M_{p,1} = 2$ and $M_{p,2} = 4 M_\odot$. Assuming a continuous IFMR, we therefore construct a three-component, piecewise linear model with four free parameters: three separate slopes for each regime and a y-intercept that translates the relation vertically.

Figure 15 demonstrates the parameterization of \mathbf{G} . We follow the recommendation of Hogg et al. (2010) to parametrize linear relations in terms of the angle each line makes with the horizontal and the perpendicular distance of the line from the origin (ϕ and b_\perp), instead of the slope and intercept (m and b):

$$\mathbf{G} = \begin{cases} \tan \phi_1 (M_i) + b_1 & : M_i < M_{p,1} \\ \tan \phi_2 (M_i) + b_2 & : M_{p,1} < M_i < M_{p,2} \\ \tan \phi_3 (M_i) + b_3 & : M_{p,2} < M_i. \end{cases} \quad (21)$$

To ensure the model is continuous, we have:

$$\begin{aligned} b_2 &= (\tan \phi_1 - \tan \phi_2) M_{p,1} + b_1 \\ b_3 &= (\tan \phi_2 - \tan \phi_3) M_{p,2} + b_2 \end{aligned} \quad (22)$$

Combined with our two WD mass distribution parameters, the piecewise function can then be expressed in

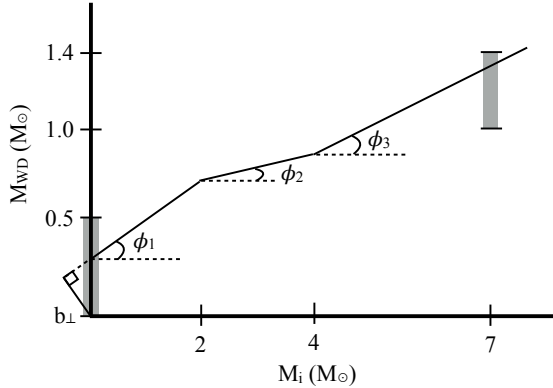


FIG. 15.— The form of our IFMR (\mathbf{G}) is a three-component, piecewise linear model that we parameterize with the perpendicular distance of the line from the origin (b_{\perp}) and three horizontal angles (ϕ_1 , ϕ_2 , and ϕ_3). We also show model priors from Equation 25; \mathbf{G} must go through the gray regions at $M_i = 0$ and $7 M_{\odot}$. Our priors from Equation 24 require that all three horizontal angles are positive and less than $\pi/2$ radians.

terms of our four IFMR model parameters:

$$\begin{aligned} \Theta &= (\Theta_{\text{WD}}, \Theta_{\text{IFMR}}) \\ \Theta &= (\mu_{\text{WD}}, \sigma_{\text{WD}}, b_{\perp}, \phi_1, \phi_2, \phi_3), \end{aligned} \quad (23)$$

where $b_{\perp} = b_1 \cos \phi_1$. We include priors on our model parameters to ensure that the model IFMR is an increasing function:

$$\begin{aligned} \phi_1 &\in [0, \pi/2] \\ \phi_2 &\in [0, \pi/2] \\ \phi_3 &\in [0, \pi/2]. \end{aligned} \quad (24)$$

Finally, we add a prior to our model so that \mathbf{G} intercepts the y-axis between 0 and $0.5 M_{\odot}$, and a second prior that ensures that a $7.0 M_{\odot}$ star produces a WD with a mass between 1.0 and $1.4 M_{\odot}$:

$$\begin{aligned} 0 &< \mathbf{G}(0.0 M_{\odot}) < 0.5 M_{\odot} \\ 1.0 &< \mathbf{G}(7.0 M_{\odot}) < 1.4 M_{\odot}. \end{aligned} \quad (25)$$

These two constraints are shown by the gray regions in Figure 15.

4.4. Testing the Model with Mock Data

We generate a set of mock observations using a test IFMR, then compare the derived constraints obtained from our model to the input IFMR. We first choose a test set of parameters for our IFMR and generate a mock sample of 20 wide DWDs. Table 6 summarizes the distributions these mock data are drawn from.

The first WD in the pair is randomly assigned a mass from a truncated Gaussian distribution. The second WD’s mass is then obtained based on a mass ratio, q , randomly generated from another Gaussian distribution. We determine M_i using the model IFMR, then the pre-WD lifetimes for each WD with the function shown in Figure 12.

τ_{cool} for the less-massive, slower-evolving WD is selected from a flat distribution in log space between 10 Myr and 1 Gyr. Following Equation 2, we then assign the more massive WD the τ_{cool} of its companion plus the difference in pre-WD lifetimes.

The WDs are then “observed.” Masses and cooling ages are randomly selected from Gaussian distributions centered on the true (mock) values, with standard deviations of $0.03 M_{\odot}$ in WD mass and 10% in τ_{cool} (these uncertainties are typical of WD spectral fits). Finally, the observed WD masses and τ_{cool} and their associated uncertainties are used as inputs for our Bayesian model.

We use 32 separate chains in `emcee`, running for 10,500 steps, the first 500 steps are a “burn-in,” which we throw away then check to make sure the chains have converged. Figure 16 shows our input model (black, dashed) and 50 randomly drawn samples (gray) from the posterior distribution of model parameters. Importantly, the posterior samples are evenly distributed around the input IFMR. The spread in the posterior samples indicate the constraints these mock systems place on the IFMR.

TABLE 6
MOCK DATA PARAMETERS

Parameter	Input Distribution	Range
M_1	$\mathcal{N}(\mu = 0.75 M_{\odot}, \sigma = 0.15 M_{\odot})$	(0.6, 1.2)
q	$\mathcal{N}(\mu = 1.0, \sigma = 0.15)$	(0.45, 1.0)
$\log \tau_2$	\mathcal{U}	(7.0, 9.0)
Mock IFMR Parameters		
Θ_{IFMR}	(0.1, 0.1, 0.38, 0.05)	

NOTE. — \mathcal{N} is a Gaussian distribution with mean μ and standard deviation σ . \mathcal{U} is the uniform distribution. The range dictates where the distributions are truncated. The model parameters, Θ_{IFMR} are defined in Equation 23. Observational uncertainties of $0.03 M_{\odot}$ are assigned to M_{WD} and 10% to τ_{cool} .

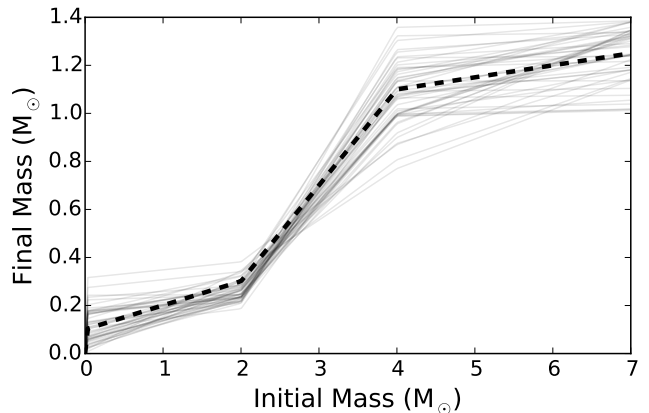


FIG. 16.— The input mock IFMR is shown by the black dashed line, while samples from the posterior are semi-transparent in gray. The posterior samples are evenly distributed around the input distribution.

Figure 17 shows the covariances between the four IFMR parameters in our model. Our model, for this particular combination of input parameters and mock wide DWDs, is able to constrain only certain regions of phase space. Figure 16 shows why; since there are no $<0.5 M_{\odot}$ WDs in the sample, our model is insensitive to the exact form of the first component in our piecewise linear model. Similarly, there are few $>1.0 M_{\odot}$ WDs in our sample, and the uncertainties in τ_{cool} estimates for these are of order the differences in the pre-WD lifetimes (however, these

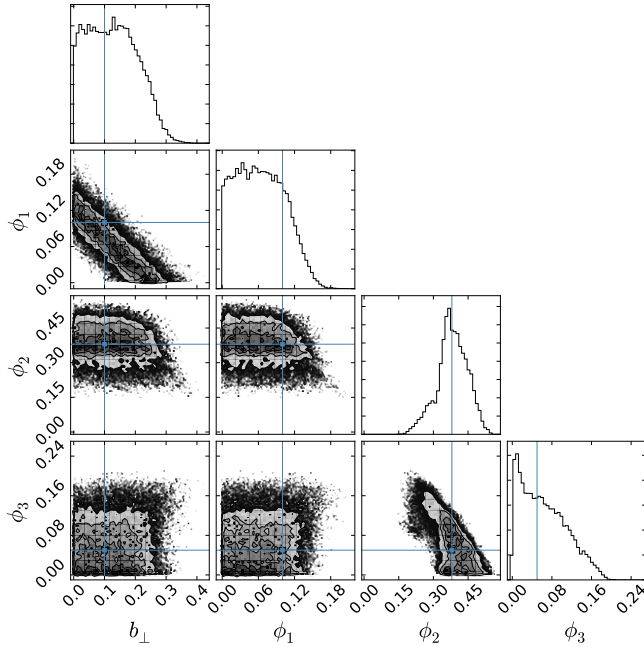


FIG. 17.— Covariances between the four parameters in Θ_{IFMR} in our model for our mock data set. Lines indicate the input values for our parameters. Our posterior distributions are centered around the input parameters, indicating that our model converged to the correct solutions.

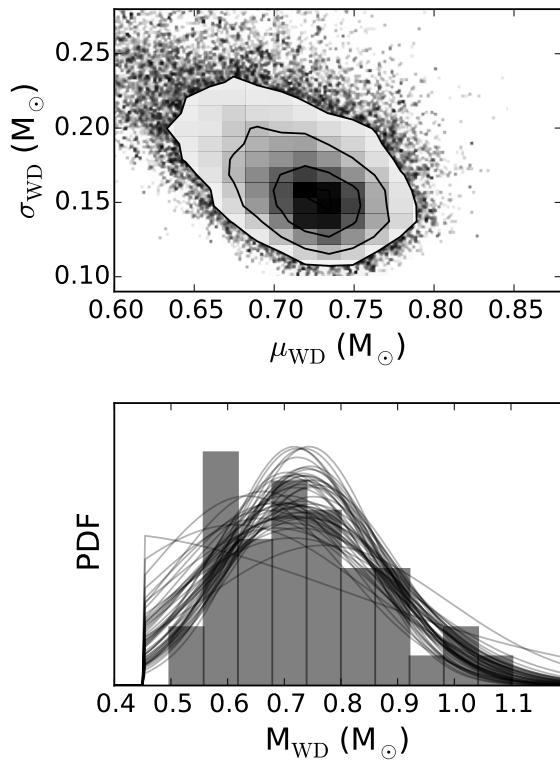


FIG. 18.— The top panel shows the covariance between the WD mass distribution model parameters μ_{WD} and σ_{WD} for our mock data set. The bottom panel shows a normalized histogram of the WD masses in our test sample. Lines show samples from the posterior distribution of model parameters.

data can constrain ϕ_2 , the second piecewise linear component of our model). For the set of mock wide DWDs shown here, the constraints are most stringent between roughly 2 and 3 M_{\odot} .

The top panel of Figure 18 shows the covariance between the two model parameters describing the WD mass distribution. Although our model is too simple to exactly reproduce the input WD masses, the bottom panel shows that posterior samples from our model (lines) approximate the input WD mass distribution (histogram).

4.5. Applying the Model to Wide DWDs

We applied our parametric model to our sample of wide DWDs using `emcee`. We check the 32 separate Markov chains to make sure they have converged. Here again, we throw away the first 500 steps and run the model for another 50000 steps. We make samples from our posterior distribution publicly available for download.¹⁴ Figure 19 shows selected samples from the posterior distribution of model parameters. The posterior samples converge between 2 and 4 M_{\odot} .

Reassuringly, this mass range corresponds to ≈ 0.5 – $0.8 M_{\odot}$ WDs, roughly the masses of the WDs in our sample (see Table 4). Smaller M_i produce WDs too low-mass to be found in our sample, and our method is not as sensitive to the small differences in the pre-WD lifetimes of more massive stars.

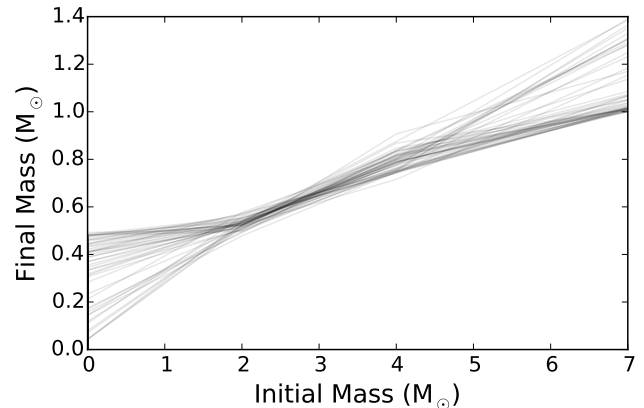


FIG. 19.— Samples from the posterior distribution for our fiducial model are semi-transparent in gray. The model converges for the second linear component ($M_i = 2$ – $4 M_{\odot}$), but diverges outside of this mass range.

The covariances between the different model parameters are shown in Figure 20. These confirm that the parameters have converged. In particular, the slope of the second piecewise linear component of our model, ϕ_2 , is well constrained, and the covariance between b_{\perp} and ϕ_1 indicates that the model is well constrained near the pivot point at $M_i = 2 M_{\odot}$.

4.6. A Test of the Number of Model Parameters

To test the dependence of our results on our model, we extend our model by allowing the pivot points to vary. We then have a model with eight parameters: μ_{WD} , σ_{WD} ,

¹⁴ <http://dx.doi.org/10.6084/m9.figshare.1572148>

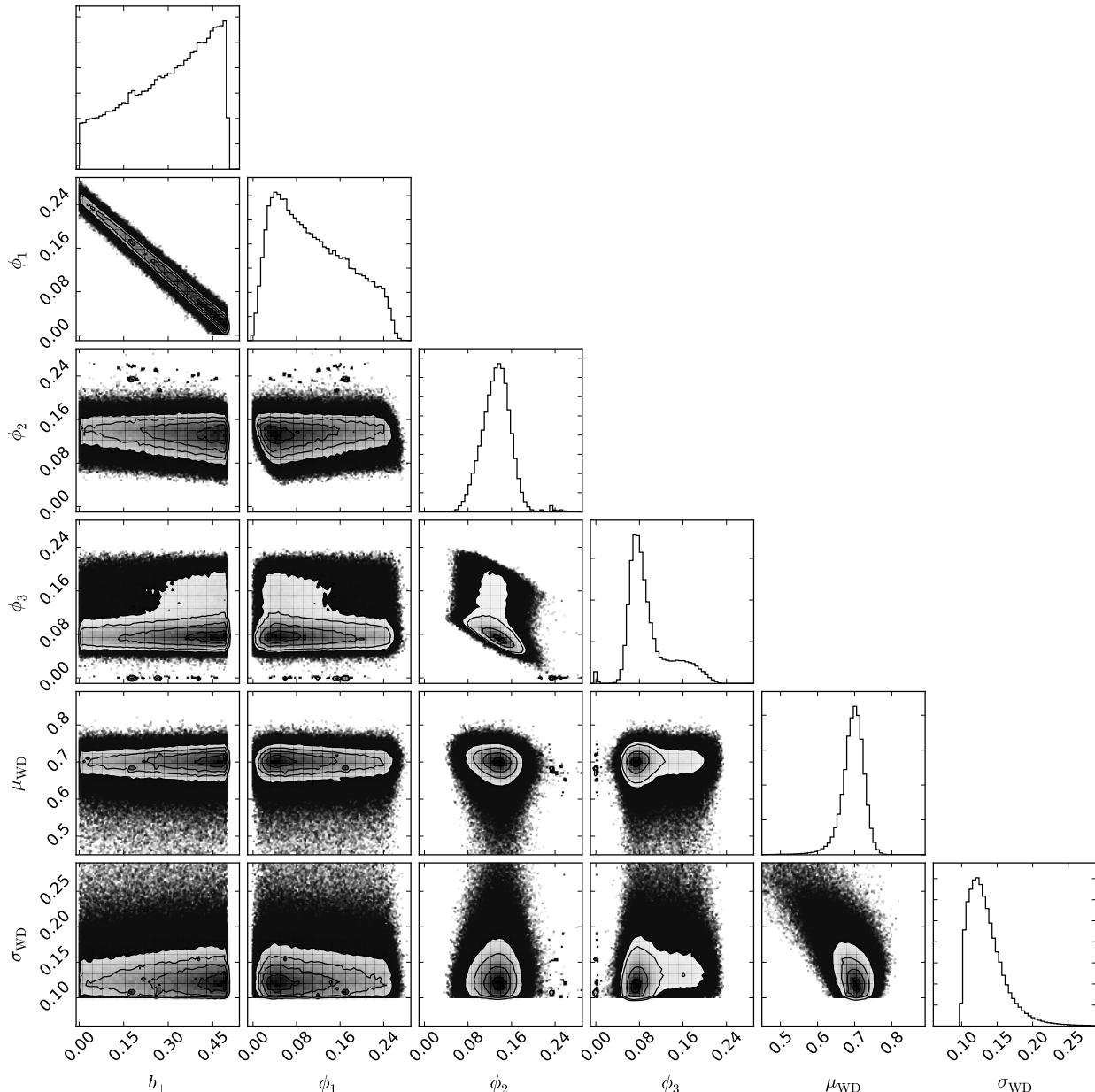


FIG. 20.— Covariances of the model parameters for our model applied to our sample of wide DWDs.

ϕ_1 , ϕ_2 , ϕ_3 , b_\perp , $M_{p,1}$, and $M_{p,2}$. We keep the same priors on the first six parameters in Equations 18, 24, and 25, and add flat priors on the pivot masses:

$$\begin{aligned} M_{p,1} &\in [1.5, 2.5] \\ M_{p,2} &\in [3.5, 4.5]. \end{aligned} \quad (26)$$

Figure 21 shows the results when we apply this eight-parameter model. Even with this more flexible model, the posterior distribution converges to a narrow distribution in M_{WD} for $M_i = 2-4 M_\odot$, suggesting that this convergence is not a result of our original choice to fix the pivot points.

In model parameter space, however, the masses at which the IFMR pivots do not converge. This can be seen in Figure 21: the pivot points vary across the whole allowed range. Perhaps with a future, larger data set,

this model will be able to constrain $M_{p,1}$ and $M_{p,2}$, but the current sample of wide DWDs cannot.

Because our original six-parameter model reasonably represents the constraints from our DWD sample and the Markov chains converge to a region in parameter space, we choose that model as our fiducial model for the remainder of our analysis.

5. DISCUSSION

5.1. Comparison to Theoretical Predictions

While stellar evolution codes still disagree significantly on the functional form of the IFMR, major divergences typically occur after the first thermal pulse, and codes generally produce similar core masses at the 1TP (Kalirai et al. 2014). Furthermore, one of the primary expectations from theory is that the core mass will not diminish

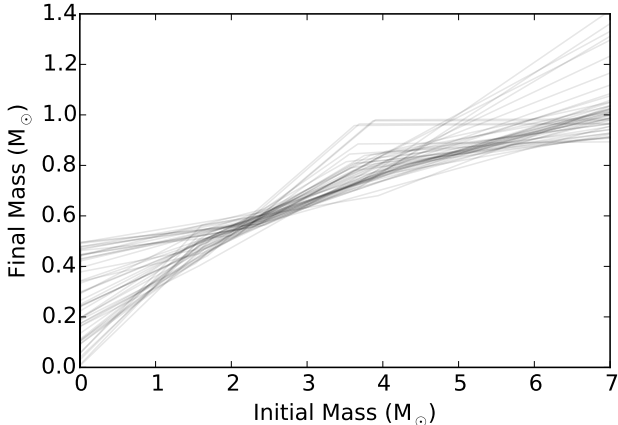


FIG. 21.— Samples from the posterior distribution for our eight-parameter model in which the pivot points for our three-component, piecewise model are allowed to vary. The results are consistent with those from the six-parameter model: our DWDs constrain the IFMR between $\approx 2\text{--}4 M_{\odot}$.

on the TP-AGB (e.g., Karakas et al. 2002). This provides a significant sanity check for any observationally derived IFMR: for a given M_i , the resulting WD should be at least as massive as the 1TP core mass.

We compared samples from the posterior distribution from our fiducial model to the 1TP core masses obtained from the theoretical relations of Dominguez et al. (1999), Weiss & Ferguson (2009), and Kalirai et al. (2014). Reassuringly, between 2 and $4 M_{\odot}$, our fiducial model constrains the IFMR to be above these relations.

Evolving from the 1TP to produce a WD is computationally challenging. The pulses that give the TP-AGB phase its name are due to thermal instabilities in the helium-burning shell of the AGB star (Schwarzschild & Härm 1965). These pulses are suspected to form a temporary convective zone within the He inter-shell region. This leads to the so-called third dredge-up, in which the convective envelope extends into the inter-shell region, mixing heavier elements into the outer envelope (Iben 1975). This sequence of successive dredge-up events and overshooting naturally explain the observed C abundances in AGB stars (cf. discussion in Herwig 2000).

Although convective overshooting has been seen in three-dimensional numerical simulations, such calculations are currently only possible for small regions of a stellar atmosphere over small timescales (e.g., Freytag et al. 2012). For now, stellar evolution predictions are typically limited by the ability of 1D models, which rely on some form of mixing-length theory (Böhm-Vitense 1958) combined with a prescription for convective overshooting (cf. Herwig 2000, and references therein), to calculate accurately the energy transport during these pulses. This can cause problems. For example, 1D approximations can lead to large radiation pressures developing at the base of the convective envelope, which can in turn lead to unphysically large (supersonic) radial velocities. One way to deal with this involves decreasing the opacity profiles by hand in these regions (e.g., Renedo et al. 2010; Pignatari et al. 2013).

With these caveats in mind, we present in Figure 22 three IFMRs produced by different stellar evolution

codes; the major differences between them stem from the treatments of dredge-up and wind mass loss. Renedo et al. (2010) argue, based on the theoretical results of Canuto (1998) and observations of *s*-process abundances by Lugaro et al. (2003), that the third dredge-up should be suppressed. In this scenario, the He core grows continuously, its mass only limited by the reduction of the envelope due to stellar winds, as described using the prescription of Vassiliadis & Wood (1993).

The Kalirai et al. (2014) IFMR uses the AGB models of Marigo et al. (2013), which improve the treatment of the onset of the third dredge-up and the calculation of opacities. However, the resulting IFMR is still dependent upon a prescription for the dredge-up efficiency (Kalirai et al. 2014) use the prescription of Karakas et al. 2002) and the wind mass loss. Kalirai et al. (2014) calibrate their prescriptions by defining ignorance parameters and then finding the best fit ignorance parameters to match the observed open cluster constraints.

Finally, Weiss & Ferguson (2009) use the exponential overshooting prescription of Herwig et al. (1997). On the AGB, these authors use the wind mass loss prescription of Wachter et al. (2002) for C-rich AGB stars and the prescription of van Loon et al. (2005) for O-rich AGB stars. The Weiss & Ferguson (2009) simulations show little core growth on the TP-AGB, resulting in less massive WDs for a given M_i compared with the models produced by Renedo et al. (2010) and Kalirai et al. (2014).

Figure 22 includes our posterior samples with these three theoretical IFMRs. For $M_i = 2\text{--}4 M_{\odot}$, our model converges to a region of parameter space that suggests that the IFMR may lie between the higher final-mass models of Renedo et al. (2010) and Kalirai et al. (2014) and the lower final-mass model of Weiss & Ferguson (2009). We may not yet be able to place stringent constraints on wind-mass-loss models and dredge-up efficiencies with the available data, but Figure 22 suggests that DWDs may eventually provide important new observational tests for stellar evolution codes.

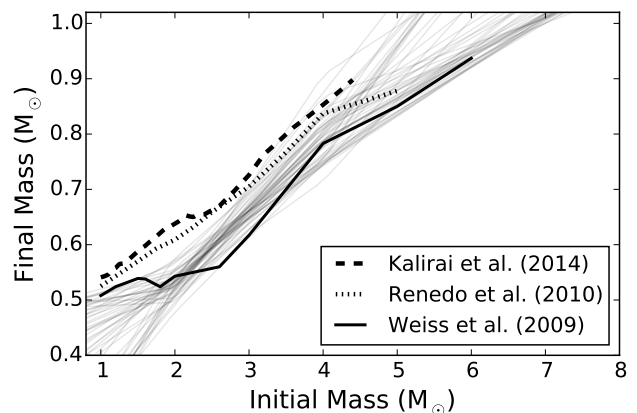


FIG. 22.— A comparison between samples from the posterior distribution from our fiducial model (gray lines) and theoretical IFMRs obtained from three separate stellar evolution codes. The differences between the codes are due primarily to treatment of the dredge-up and wind mass loss.

5.2. Comparison to Other Observational Constraints

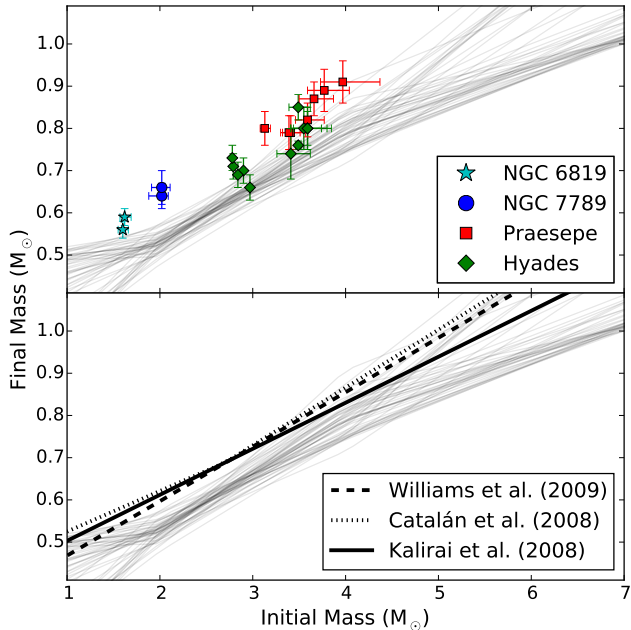


FIG. 23.— The top panel shows samples from the posterior distribution for our model (gray lines) and the observational constraints generated by WDs in four older open clusters (from Kalirai et al. 2014). The bottom panel compares the same posterior samples to the semi-empirical linear fits of Catalán et al. (2008), Kalirai et al. (2008), and Williams et al. (2009).

The most commonly used method for constraining the IFMR is that pioneered by Sweeney (1976). Here, the WDs are members of open clusters for which reliable ages can be obtained from e.g., isochrone fitting. There are at least two important limitations to consider when discussing this method. The first is that even for the nearby, well-studied open clusters that are generally used in these studies, significant disagreements about the stars’ ages are not unusual. Furthermore, the techniques employed to obtain these ages differ, so that the constraints on the IFMR depend on different sets of systematic effects.

The second is that most easily accessible open clusters are young, with ages $\ll 1$ Gyr, so that only the most massive stars have evolved off the main-sequence. There are four notable exceptions: NGC 6819, NGC 7789, the Hyades, and Praesepe are all old enough for their $\approx 2\text{--}4 M_{\odot}$ members to have evolved into WDs. Kalirai et al. (2014) recently re-analyzed the 18 WDs identified in these four clusters using improved WD atmospheric models. These data are shown in the top panel of Figure 23. Our results are consistent with those derived from WDs in the Hyades, but the initial masses for WDs in NGC 7789 and Praesepe are systematically lower than our posterior samples.¹⁵

Various authors have pointed out that metallicity could lead to a natural spread in the IFMR (e.g., Kalirai et al. 2005). However, the four clusters hosting the WDs in Figure 23 all have near-solar metallicities,¹⁶ while we

also expect the DWDs in our sample to have roughly solar metallicity (see Section 4.1.2). While Meng et al. (2008) and Romero et al. (2015) showed that metallicity-dependent mass-loss rates can result in WDs with masses varying by as much as $0.2 M_{\odot}$, the range is principally due to cases of extremely low or high metallicities. For metallicities near solar, variations in $M_{\text{WD}} \lesssim 0.05 M_{\odot}$ (see figure 1 in Meng et al. 2008 and figure 4 in Romero et al. 2015). Metallicity differences are therefore unlikely to explain the discrepancy between our constraints and the WDs in these open clusters.

Instead, the difference could stem from uncertainties in the cluster ages. Kalirai et al. (2014) followed Claver et al. (2001) in adopting the *Hipparchos*-derived Hyades age of 625 Myr (Perryman et al. 1998) for Praesepe.¹⁷ By contrast, when fitting metallicity-specific isochrones to Praesepe, Salaris et al. (2009) found an age ranging from $\approx 450\text{--}650$ Myr. The inclusion of convective overshooting, which extends stellar lifetimes, accounts for the difference. If, instead of 625 Myr, the Hyades and Praesepe are 550 Myr, the corresponding data points in Figure 23 would all shift right, toward higher M_i , by $\approx 0.2\text{--}0.3 M_{\odot}$. These constraints would then be consistent with samples from our posterior distribution.¹⁸

The discrepancy with the two WDs in NGC 7789 could also be due to an inaccurate cluster age. Kalirai et al. (2014) adopt the age of 1.4 Gyr obtained by Kalirai et al. (2008) from isochrone fits. However, isochrone-derived ages for this cluster vary noticeably in the literature, ranging from 1.1 Gyr (Mazzei & Pigatto 1988) to 1.6 Gyr (Gim et al. 1998). A modestly younger age of 1.2 Gyr for NGC 7789 increases the derived M_i by $\approx 0.2 M_{\odot}$, enough that these data also become consistent with samples from our posterior distribution.

There are a number of other possibilities for the differences we see in Figure 23. Our piecewise-linear model might be inappropriate because there is significant structure in the IFMR for $M_i = 2\text{--}4 M_{\odot}$. Some of the WDs in either the open cluster or wide DWD data may have unresolved binary companions that affected their evolution, and therefore should not be used to constrain the IFMR. To identify the source(s) of this discrepancy, progress needs to be made with both methods: we need more complex models than that presented here for the IFMR, combined with larger sets of wide DWDs, as well as new WDs in older open clusters.

The bottom panel of Figure 23 shows that our posterior samples lie significantly below the semi-empirical IFMRs of Catalán et al. (2008), Kalirai et al. (2008), and Williams et al. (2009). These authors use somewhat different WD samples and spectroscopic solutions in generating their linear fits, but for $M_i = 2\text{--}4 M_{\odot}$, the constraints are obtained predominantly with the WDs shown in the top panel of Figure 23.

Considering the uncertainties in the ages of the clusters hosting these WDs, we suggest that these semi-empirical relations be used with caution for $M_i = 2\text{--}4 M_{\odot}$. Samples from the posterior distribution from our model may be

¹⁵ We ignore the WDs in NGC 6819, since these evolved from $< 2 M_{\odot}$ stars, outside the mass range to which we are sensitive.

¹⁶ NGC 6819: $[\text{Fe}/\text{H}] = -0.02 \pm 0.02$ (Lee-Brown et al. 2015); NGC 7789: $+0.03 \pm 0.07$ (Overbeek et al. 2015); Praesepe: $+0.16 \pm 0.05$ (Carrera & Pancino 2011); Hyades: $+0.11 \pm 0.01$ (Carrera & Pancino 2011).

¹⁷ For a recent discussion of the evidence that the two clusters are indeed the same age, see Douglas et al. (2014).

¹⁸ Brandt & Huang (2015) recently argued that if stellar models accounting for rotation are used in the isochrone fitting, both clusters are ≈ 800 Myr, illustrating just how much uncertainty remains about the age of two of the nearest, best-studied open clusters.

more accurate within this M_i mass range.

6. CONCLUSIONS

In an effort to provide new, independent constraints on the IFMR, we began by conducting a comprehensive search for wide DWDs in the SDSS DR9 photometric catalog. Using two separate methods, we identified 65 new candidate systems. By combining these pairs with those already in the literature, we assembled a sample of 142 candidate and confirmed wide DWDs.

To confirm the WD nature of the stars in these pairs, and to obtain accurate mass and τ_{cool} measurements for them, we engaged in a spectroscopic campaign using the 3.5-m APO telescope (and also collected spectra from the literature). Our targets included new systems identified in Andrews et al. (2012), those photometrically selected from DR9, and literature pairs that lacked spectroscopy. The contamination by non-WDs was extremely low: only one of the 97 objects for which we obtained spectra was not a WD. Fitting WD model atmospheres to our spectra gave us $\log g$ and T_{eff} values; these were then converted to M_{WD} and τ_{cool} for each star.

In addition to 27 DA/DA pairs, our campaign identified a number of interesting systems that cannot be used to constrain the IFMR. We confirmed the nature of the second known DA/DB system, SDSS J0849+4712 (CDDS15), and identified SDSS J2355+1708 as the third DA/DB DWD. DBs may evolve from H-deficient post-AGB stars (Althaus et al. 2005), and it is unclear whether the same IFMR applies to these stars as to DA WDs and their progenitors. We found four new DC WDs with DA companions (we also confirm the nature of another previously identified DA/DC system); the lack of absorption features makes it impossible to determine the mass of the DCs from spectra alone. We identify four new candidate DA/DAH pairs, and confirm the nature of three previously known systems; the DAH spectra cannot be fit with DA atmospheric models, and in general require higher-resolution and/or better S/N spectra to confirm their nature.

Finally, we identify two candidate triple systems: PG 0901+140 (based on the anomalously low mass of one of its components, this system could be a triple degenerate) and J2047+0022B (which was previously identified by Silvestri et al. (2006) as an unresolved DQ+K7 binary). Because of the potential for mass transfer in the unresolved pair, candidate triple systems such as these had to be excluded from our efforts to constrain the IFMR.

We divided our double DAs into high- and low-fidelity pairs, labeling the DWDs with mass uncertainties $>0.1 M_{\odot}$ in at least one WD as low-fidelity. These pairs have spectra good enough to identify objects as DAs, but too poor to obtain accurate fits to model atmospheres. We also considered the spectroscopic distances to each WD in these candidate DWDs, and designated pairs with a distance difference $>25\%$ as low-fidelity. Finally, we removed from our high-fidelity sample DWDs for which the more massive WD appeared to have a shorter τ_{cool} than its less-massive companion, as this goes against standard expectations from stellar evolution. Combining our high-fidelity pairs with DWDs from Baxter et al. (2014) for which we lacked spectroscopic data, we obtained a sample of 19 DWDs with which to constrain the IFMR.

Because the members of wide binaries are co-eval and

evolve independently (i.e., without mass transfer affecting their evolutionary pathways), the age of each WD in a DWD is the same and is the sum of each WD's τ_{cool} and pre-WD lifetime. Using this as a starting point, we developed a hierarchical Bayesian framework that tests the likelihood that any particular IFMR accounts for the observed masses and cooling ages, and corresponding uncertainties, of a wide DWD. We then constructed a parametrized form of the IFMR, choosing a continuous, piecewise-linear function with pivot points at 2 and 4 M_{\odot} . We also included a model for the underlying WD mass distribution, which we varied simultaneously with the IFMR parameters.

We first tested our model on a set of mock wide DWDs and successfully recovered our input IFMR. We then applied our model to our 19 high-fidelity DWDs, using a Markov Chain Monte Carlo approach to find the region of parameter space implied by the data. We make samples from our posterior distribution of parameters available for download. The resulting constraints are comparable to previous constraints on the IFMR obtained using WDs in open clusters. However, our results produce larger M_i than previous observations (or alternatively, we found that stars of a given M_i produce less massive WDs). Importantly, our constraints are most sensitive to $M_i = 2-4 M_{\odot}$, a regime that the open cluster data have difficulty testing. We found no improvement when we tested an expanded model in which the pivot points vary; our original model with fixed pivot points is sufficient to describe our current set of DWDs.

Our model can be expanded to include other constraints, including those from open cluster WDs, globular cluster WD cooling tracks, and Sirius-like binaries. Because each of these methods has their own associated systematic uncertainties, including these in a statistically responsible way is not straightforward, however.

Our three-component, piecewise linear model is only an approximation for the true, physical IFMR. Ultimately, we would like to be able to constrain physically meaningful stellar evolution parameters. Kalirai et al. (2014) recently performed such an analysis using the WDs presented in Figure 23. Our method here could similarly be expanded to constrain stellar evolution directly. For example, the form of the IFMR within the $M_i = 2-4 M_{\odot}$ range is sensitive to physics on the TP-AGB. DWD data may be precise enough to place important constraints on uncertain dredge-up and overshooting physics. We leave this to future work.

In our search for new DWDs, we relied on SDSS photometry combined with proper motion measurements to identify WD candidates, while masses and τ_{cool} were derived from fits to WD template spectra. With precision astrometry from the *Gaia* space telescope, identifying WDs and matching them with common proper motion companions will be significantly easier. Furthermore, as pointed out by Carrasco et al. (2014), data from the BP and RP spectrophotometers, combined with distance measurements and a mass-radius relation, will provide T_{eff} and M_{WD} for every WD identified. These authors estimate *Gaia* will find some 250,000 to 500,000 WDs. We do not know the space density of wide DWDs in the Galaxy, but it is hard to escape the conclusion that *Gaia* will identify hundreds to thousands of new wide DWDs. With a measured T_{eff} and M_{WD} for the WDs in each of

these pairs, these wide DWDs will potentially revolutionize our understanding of the IFMR.

We thank the referees for their comments which led to improvements in the manuscript. We thank the observing specialists for their help with the APO observations. We thank P. Bergeron for fitting the DB WDs in our sample and D. Koester for providing us with VLT spectra of several of the WDs discussed here. We thank Lars Bildsten, Silvia Catalán, Falk Herwig, David Hogg, Marcelo Miller Bertolami, Rodolfo Montez, Jr., and Adrian Price-Whelan for stimulating and helpful discussions. M.A.A., M.K., and A.G. gratefully acknowledge the support of the NSF and NASA under grants AST-1255419, AST-1312678, and NNX14AF65G, respectively.

This work made use of the *yeti* cluster at the Columbia University Shared Research Computing Facility, which is supported by NIH Research Facility Improvement Grant 1G20RR030893-01 and matching funds from New York State/the Empire State Development’s Division of Science, Technology and Innovation (NYSTAR) under Contract C090171.

Funding for SDSS-III has been provided by the Alfred P. Sloan Foundation, the Participating Institutions, the National Science Foundation, and the U.S. Department of Energy Office of Science. The SDSS-III web site is <http://www.sdss3.org/>.

SDSS-III is managed by the Astrophysical Research Consortium for the Participating Institutions of the SDSS-III Collaboration including the University of Arizona, the Brazilian Participation Group, Brookhaven National Laboratory, University of Cambridge, Carnegie Mellon University, University of Florida, the French Participation Group, the German Participation Group, Harvard University, the Instituto de Astrofísica de Canarias, the Michigan State/Notre Dame/JINA Participation Group, Johns Hopkins University, Lawrence Berkeley National Laboratory, Max Planck Institute for Astrophysics, Max Planck Institute for Extraterrestrial Physics, New Mexico State University, New York University, Ohio State University, Pennsylvania State University, University of Portsmouth, Princeton University, the Spanish Participation Group, University of Tokyo, University of Utah, Vanderbilt University, University of Virginia, University of Washington, and Yale University.

APPENDIX

Our spectroscopic campaign uncovered a number of interesting DWDs that could not be used to constrain the IFMR. These include two systems in which a DA is paired with a DB WD, which is a WD lacking an optically thick H layer and with $T_{\text{eff}} \gtrsim 12,000$ K. SDSS J0849+4712 (CDD515) was previously identified by Baxter et al. (2014) as the second known DA/DB system after L 151-81 A/B (Oswalt et al. 1988). Here we report J2355+1708 as the third identified wide DA/DB DWD.

The DBs in these systems, SDSS J0849+4712B (CDD515-A) and J2355+1708B, are shown in Figure 24. The fit results for these stars in Table 3 were provided by P. Bergeron (priv. communication). DBs probably form through a different channel than DAs. They may evolve from H-deficient post-AGB stars (Althaus et al.

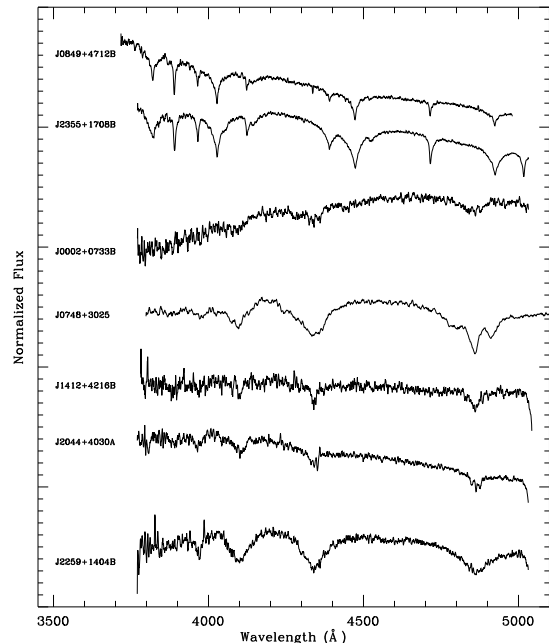


FIG. 24.— The two top spectra are for the DBs in our sample: J0849+4712B (CDD515-A) and J2355+1708B. The other spectra are for five DAHs: J0002+0733B, J0748+3025, J1412+4216B, J2044+4030A, and J2259+1404B. We do not include the SDSS spectra for PG 1258+593B and J1314+1732A, which show Zeeman splitting in the $H\alpha$ line, but not in the higher order Balmer lines.

2005), and it is unclear whether the same IFMR applies to these stars.

As DBs cool to $T_{\text{eff}} \lesssim 12,000$ K, they can no longer ionize He. They are then known as DC WDs and characterized by their featureless blackbody spectra. The lack of absorption features makes it impossible to determine the mass of these DC WDs from spectra alone. We identify four DC WDs in our sample: LP 549-32, J0029+0015A (CDD52), J0344+1510A, and J1544+2344B. GD 559 was previously identified as a DA/DC wide pair by Farihi et al. (2005). Due to their cool temperatures, the spectra of these objects generally have a low S/N.

Magnetic DAs (DAHs) are identified by Zeeman splitting in the Balmer lines. We have identified four new candidate DAHs: J0002+0733B, J1314+1732A, J1412+4216B, and J2044+4030A. We also confirm the DAH nature of three previously identified DAH WDs in wide pairs: PG 1258+593B (Girven et al. 2010), J0748+3025 (CDD511 Dobbie et al. 2013; Baxter et al. 2014) J2259+1404B (CDD52 Baxter et al. 2014). Spectra for several of these are shown in Figure 24. Since DA atmospheric models cannot be used here, we only include spectroscopic fits to the DAHs’ companions in Table 7.

We label the DA/DC and DA/DAH systems as candidates in Table 7 because higher-resolution and/or better S/N spectra are required to confirm the nature of the non-DAs in these pairs.

The “B” component of the wide DWD J2047+0021B was identified by Silvestri et al. (2006) as a carbon atmosphere WD (DQ) with a K7 companion. This would make it the second such triple system composed of two WDs and a K star, after CDD530 (Baxter et al. 2014). We list J2047+0021 as a candidate triple system in Table

7.

Finally, while it is possible to form single WDs with masses as low as $0.45 M_{\odot}$ (Kilic et al. 2007), observations of WDs with $M_{\text{WD}} < 0.45 M_{\odot}$ indicate a binary fraction $\gtrsim 80\%$ (Brown et al. 2011), suggesting that the low-mass WDs in several of our systems are in fact unresolved binaries. These systems are listed as candidate triple systems in Table 7. This list includes the two known systems, G 21-15 (Farihi et al. 2005) and Gr 576/577 (Maxted et al. 2000), which are hierarchical triples composed of a close pair of WDs with a degenerate tertiary body in a larger orbit. In both systems, our spectroscopic fits return $\approx 0.45 M_{\odot}$ for the unresolved close pair. Addi-

tionally, PG 0901+140A (with $M_{\text{WD}} = 0.47 \pm 0.04 M_{\odot}$) may be an unresolved degenerate pair. Because of the potential for mass transfer in the unresolved pairs, these systems cannot be used to constrain the IFMR and were excluded from our analysis. We note here that our spectroscopic solutions for PG 0901+140 differ substantially from those of Farihi et al. (2005), who find that both WDs in the system are approximately $0.8 M_{\odot}$.

For completeness, we also include in Table 7 those systems for which we had only one spectrum and our one spectroscopic contaminant, the DA/A-star pair SDSS J2124–1620.

REFERENCES

- Abate, C., Pols, O. R., Izzard, R. G., Mohamed, S. S., & de Mink, S. E. 2013, *A&A*, 552, A26
- Abazajian, K. N. et al. 2009, *ApJS*, 182, 543
- Ahn, C. P. et al. 2012, *ApJS*, 203, 21
- Althaus, L. G., Serenelli, A. M., Panei, J. A., Córscico, A. H., García-Berro, E., & Scóccola, C. G. 2005, *A&A*, 435, 631
- Andrews, J. J., Agüeros, M. A., Belczynski, K., Dhital, S., Kleinman, S. J., & West, A. A. 2012, *ApJ*, 757, 170
- Asplund, M., Grevesse, N., Sauval, A. J., & Scott, P. 2009, *ARA&A*, 47, 481
- Baxter, R. B. et al. 2014, *MNRAS*, 440, 3184
- Bergeron, P., Saffer, R. A., & Liebert, J. 1992, *ApJ*, 394, 228
- Böhm-Vitense, E. 1958, *ZAp*, 46, 108
- Boss, A. P. 1988, *Comments on Astrophysics*, 12, 169
- Brandt, T. D., & Huang, C. X. 2015, *ApJ*, 807, 24
- Brown, J. M., Kilic, M., Brown, W. R., & Kenyon, S. J. 2011, *ApJ*, 730, 67
- Canuto, V. M. 1998, *ApJ*, 508, L103
- Carrasco, J. M., Catalán, S., Jordi, C., Tremblay, P.-E., Napiwotzki, R., Luri, X., Robin, A. C., & Kowalski, P. M. 2014, *A&A*, 565, A11
- Carrera, R., & Pancino, E. 2011, *A&A*, 535, A30
- Casali, M. et al. 2007, *A&A*, 467, 777
- Catalán, S. 2015, in *Astronomical Society of the Pacific Conference Series*, Vol. 493, 19th European Workshop on White Dwarfs, ed. P. Dufour, P. Bergeron, & G. Fontaine, 325
- Catalán, S., Isern, J., García-Berro, E., & Ribas, I. 2008, *MNRAS*, 387, 1693
- Claver, C. F., Liebert, J., Bergeron, P., & Koester, D. 2001, *ApJ*, 563, 987
- Dhital, S., West, A. A., Stassun, K. G., & Bochanski, J. J. 2010, *AJ*, 139, 2566
- Dhital, S., West, A. A., Stassun, K. G., Schluns, K. J., & Massey, A. P. 2015, *AJ*, 150, 57
- Dobbie, P. D., Baxter, R., Külebi, B., Parker, Q. A., Koester, D., Jordan, S., Lodieu, N., & Euchner, F. 2012, *MNRAS*, 421, 202
- Dobbie, P. D. et al. 2013, *MNRAS*, 428, L16
- Dominguez, I., Chieffi, A., Limongi, M., & Straniero, O. 1999, *ApJ*, 524, 226
- Douglas, S. T. et al. 2014, *ApJ*, 795, 161
- Farihi, J., Becklin, E. E., & Zuckerman, B. 2005, *ApJS*, 161, 394
- Finley, D. S., & Koester, D. 1997, *ApJ*, 489, L79
- Fontaine, G., Brassard, P., & Bergeron, P. 2001, *PASP*, 113, 409
- Foreman-Mackey, D., Hogg, D. W., Lang, D., & Goodman, J. 2013, *PASP*, 125, 306
- Freytag, B., Ludwig, H.-G., & Steffen, M. 1996, *A&A*, 313, 497
- Freytag, B., Steffen, M., Ludwig, H.-G., Wedemeyer-Böhm, S., Schaffnerberger, W., & Steiner, O. 2012, *Journal of Computational Physics*, 231, 919
- Fuhrmann, K. 1998, *A&A*, 338, 161
- Gianninas, A., Bergeron, P., & Fontaine, G. 2005, *ApJ*, 631, 1100
- Gianninas, A., Bergeron, P., & Ruiz, M. T. 2011, *ApJ*, 743, 138
- Gim, M., Vandenberg, D. A., Stetson, P. B., Hesser, J. E., & Zurek, D. R. 1998, *PASP*, 110, 1318
- Girven, J., Gänsicke, B. T., Külebi, B., Steeghs, D., Jordan, S., Marsh, T. R., & Koester, D. 2010, *MNRAS*, 404, 159
- Girven, J., Gänsicke, B. T., Steeghs, D., & Koester, D. 2011, *MNRAS*, 417, 1210
- Goodman, J., & Weare, J. 2010, *Comm. App. Math. Comp. Sci.*, 5, 65
- Green, R. F., Schmidt, M., & Liebert, J. 1986, *ApJS*, 61, 305
- Greenstein, J. L., Dolez, N., & Vauclair, G. 1983, *A&A*, 127, 25
- Grevesse, N., & Noels, A. 1993, in *Origin and Evolution of the Elements*, ed. N. Prantzos, E. Vangioni-Flam, & M. Casse, 15–25
- Hambly, N. C. et al. 2008, *MNRAS*, 384, 637
- Herwig, F. 2000, *A&A*, 360, 952
- Herwig, F., Bloeker, T., Schoenberner, D., & El Eid, M. 1997, *A&A*, 324, L81
- Hewett, P. C., Warren, S. J., Leggett, S. K., & Hodgkin, S. T. 2006, *MNRAS*, 367, 454
- Hodgkin, S. T., Irwin, M. J., Hewett, P. C., & Warren, S. J. 2009, *MNRAS*, 394, 675
- Höfner, S. 2009, in *Astronomical Society of the Pacific Conference Series*, Vol. 414, *Cosmic Dust - Near and Far*, ed. T. Henning, E. Grün, & J. Steinacker, 3
- Hogg, D. W., Bovy, J., & Lang, D. 2010, *ArXiv e-prints*
- Iben, Jr., I. 1975, *ApJ*, 196, 525
- Kalirai, J. S., Hansen, B. M. S., Kelson, D. D., Reitzel, D. B., Rich, R. M., & Richer, H. B. 2008, *ApJ*, 676, 594
- Kalirai, J. S., Marigo, P., & Tremblay, P.-E. 2014, *ApJ*, 782, 17
- Kalirai, J. S., Richer, H. B., Reitzel, D., Hansen, B. M. S., Rich, R. M., Fahlman, G. G., Gibson, B. K., & von Hippel, T. 2005, *ApJ*, 618, L123
- Karakas, A. I., Lattanzio, J. C., & Pols, O. R. 2002, *PASA*, 19, 515
- Karovicova, I., Wittkowski, M., Ohnaka, K., Boboltz, D. A., Fossat, E., & Scholz, M. 2013, *A&A*, 560, A78
- Kepler, S. O. et al. 2015, *MNRAS*, 446, 4078
- Kilic, M. et al. 2006, *AJ*, 131, 582
- Kilic, M., Stanek, K. Z., & Pinsonneault, M. H. 2007, *ApJ*, 671, 761
- Kleinman, S. J. et al. 2013, *ApJS*, 204, 5
- Koester, D., Voss, B., Napiwotzki, R., Christlieb, N., Homeier, D., Lisker, T., Reimers, D., & Heber, U. 2009, *A&A*, 505, 441
- Kraus, A. L., & Hillenbrand, L. A. 2009, *ApJ*, 704, 531
- Lawrence, A. et al. 2007, *MNRAS*, 379, 1599
- Lee-Brown, D. B., Anthony-Twarog, B. J., Deliyannis, C. P., Rich, E., & Twarog, B. A. 2015, *AJ*, 149, 121
- Liebert, J., Bergeron, P., & Holberg, J. B. 2005, *ApJS*, 156, 47
- Lugaro, M., Herwig, F., Lattanzio, J. C., Gallino, R., & Straniero, O. 2003, *ApJ*, 586, 1305
- Marigo, P., Bressan, A., Nanni, A., Girardi, L., & Pumo, M. L. 2013, *MNRAS*, 434, 488
- Marigo, P., & Girardi, L. 2007, *A&A*, 469, 239
- Maxted, P. F. L., Marsh, T. R., Moran, C. K. J., & Han, Z. 2000, *MNRAS*, 314, 334
- Mazzei, P., & Pigatto, L. 1988, *A&A*, 193, 148
- Meng, X., Chen, X., & Han, Z. 2008, *A&A*, 487, 625
- Mohamed, S., & Podsiadlowski, P. 2007, in *Astronomical Society of the Pacific Conference Series*, Vol. 372, 15th European Workshop on White Dwarfs, ed. R. Napiwotzki & M. R. Burleigh, 397
- Mohamed, S., & Podsiadlowski, P. 2012, *Baltic Astronomy*, 21, 88
- Munn, J. A. et al. 2004, *AJ*, 127, 3034
- . 2008, *AJ*, 136, 895

- Oswalt, T. D., Hintzen, P. M., Liebert, J. W., & Sion, E. M. 1988, *ApJ*, 333, L87
- Overbeek, J. C., Friel, E. D., Jacobson, H. R., Johnson, C. I., Pilachowski, C. A., & Mészáros, S. 2015, *AJ*, 149, 15
- Paxton, B., Bildsten, L., Dotter, A., Herwig, F., Lesaffre, P., & Timmes, F. 2011, *ApJS*, 192, 3
- Paxton, B. et al. 2013, *ApJS*, 208, 4
- . 2015, *ArXiv e-prints*
- Perryman, M. A. C. et al. 1998, *A&A*, 331, 81
- Pignatari, M. et al. 2013, *ArXiv e-prints*
- Renedo, I., Althaus, L. G., Miller Bertolami, M. M., Romero, A. D., Córscico, A. H., Rohrmann, R. D., & García-Berro, E. 2010, *ApJ*, 717, 183
- Romero, A. D., Campos, F., & Kepler, S. O. 2015, *MNRAS*, 450, 3708
- Salaris, M., Serenelli, A., Weiss, A., & Miller Bertolami, M. 2009, *ApJ*, 692, 1013
- Schneider, D. P. et al. 2010, *AJ*, 139, 2360
- Schwarzschild, M., & Härm, R. 1965, *ApJ*, 142, 855
- Shu, F. H., Adams, F. C., & Lizano, S. 1987, *ARA&A*, 25, 23
- Silvestri, N. M. et al. 2006, *AJ*, 131, 1674
- Smith, M. C. et al. 2009, *MNRAS*, 399, 1223
- Sokoloski, J. L., & Bildsten, L. 2010, *ApJ*, 723, 1188
- Sweeney, M. A. 1976, *A&A*, 49, 375
- Sweigart, A. V., & Gross, P. G. 1978, *ApJS*, 36, 405
- Tremblay, P.-E., Bergeron, P., Kalirai, J. S., & Gianninas, A. 2010, *ApJ*, 712, 1345
- Tremblay, P.-E., Ludwig, H.-G., Steffen, M., & Freytag, B. 2013, *A&A*, 559, A104
- van Loon, J. T., Cioni, M.-R. L., Zijlstra, A. A., & Loup, C. 2005, *A&A*, 438, 273
- Vassiliadis, E., & Wood, P. R. 1993, *ApJ*, 413, 641
- Wachter, A., Schröder, K.-P., Winters, J. M., Arndt, T. U., & Sedlmayr, E. 2002, *A&A*, 384, 452
- Weidemann, V. 2000, *A&A*, 363, 647
- Weidemann, V., & Koester, D. 1983, *A&A*, 121, 77
- Weiss, A., & Ferguson, J. W. 2009, *A&A*, 508, 1343
- Williams, K. A., Bolte, M., & Koester, D. 2009, *ApJ*, 693, 355
- Wood, M. A. 1995, in *Lecture Notes in Physics*, Berlin Springer Verlag, Vol. 443, *White Dwarfs*, ed. D. Koester & K. Werner, 41
- York, D. G. et al. 2000, *AJ*, 120, 1579
- Zacharias, N., Urban, S. E., Zacharias, M. I., Wycoff, G. L., Hall, D. M., Monet, D. G., & Rafferty, T. J. 2004, *AJ*, 127, 3043

TABLE 7
FIT RESULTS FOR THE NON-DA/DA SPECTROSCOPIC SAMPLE

Name	Telescope	# of Fitted Balmer Lines	WD Type	S/N ^a	T_{eff} (K)	$\log g$	Distance (pc)	M_{WD} (M_{\odot})	τ_{cool} (Myr)
DA/DB Systems ^b									
J0849+4712A	APO	6	DA	28	11720±210	8.05±0.06	152±7	0.635±0.036	425±41
J0849+4712B	APO	...	DB	...	17480±310	8.08±0.06
J2355+1708A	APO	5	DA	23	10160±160	8.31±0.07	131±7	0.797±0.045	927±109
J2355+1708B	APO	...	DB	...	21470±440	8.12±0.03
Candidate DA/DAH Systems ^c									
PG 1258+593A ^d	DA	...	15160±240	8.00±0.05	65	0.61±0.03	...
PG 1258+593B	SDSS	...	DAH
J0002+0733A	APO	...	DA
J0002+0733B	APO	...	DAH
J0748+3025 ^e	SDSS	...	DAH
J1314+1732A	SDSS	...	DAH
J1314+1732B	APO	6	DA	50	12530±210	8.04±0.05	84±3	0.631±0.029	352±29
J1412+4216A	APO	6	DA	104	15420±240	8.12±0.05	79±3	0.686±0.027	220±19
J1412+4216B	APO, SDSS	...	DAH
J2044+4030A	APO	...	DAH
J2044+4030B	APO	6	DA	107	13590±240	8.00±0.05	61±2	0.607±0.026	264±22
J2259+1404A	APO	5	DA	48	25200±390	8.68±0.05	103±5	1.042±0.028	137±15
J2259+1404B ^e	APO	...	DAH
Candidate DA/DC Systems ^c									
LP 549-32	APO	...	DC
LP 549-33	SDSS	5	DA	54	6660±110	7.84±0.10	31±2	0.499±0.052	1370±179
LP 549-33	APO	5	DA	50	7090±110	8.41±0.09	24±2	0.855±0.057	3342±424
GD 559A	APO	7	DA	51	18720±290	8.14±0.05	69±3	0.701±0.028	121±13
GD 559B	APO	...	DC
J0029+0015A	SDSS	...	DC
J0029+0015B	SDSS	6	DA	33,17	9960±150	8.08±0.06	167±8	0.648±0.036	682±65
J0344+1510A	APO	...	DC
J0344+1510B	APO	6	DA	36	8300±130	7.92±0.09	64±4	0.547±0.048	871±104
J1544+2344A	SDSS	5	DA	15	9470±180	7.97±0.13	162±14	0.581±0.075	668±121
J1544+2344B	SDSS	...	DC
Candidate Triple Systems									
G 21-15 ^f	VLT	7	DA+DC	10,24,10,22	14460±210	7.66±0.04	41±2	0.448±0.018	244±10
Gr 577	APO	7	DA+DA	85	9390±130	7.74±0.05	29±1	0.461±0.023	986±33
Gr 576	APO	7	DA	73	14240±270	8.09±0.05	39±1	0.665±0.027	265±23
PG 0901+140A	APO	6	DA+DA?	67	9100±140	7.78±0.08	59±3	0.474±0.041	585±57
PG 0901+140B	APO	6	DA	39	8120±120	7.89±0.07	58±3	0.531±0.039	886±87
J2047+0021A	SDSS	5	DA	51	14330±300	8.03±0.05	140±5	0.627±0.028	236±23
J2047+0021B ^g	SDSS	...	DQ+K7
Systems With Only One Spectrum									
J0000-1051A	SDSS	5	DA	13	8590±180	8.03±0.19	161±21	0.614±0.111	933±256
J0117+2440B	SDSS	6	DA	12	17730±670	8.26±0.11	472±41	0.777±0.070	183±42
J0139+1447A	SDSS	4	DA	7	8740±250	8.29±0.31	186±49	0.779±0.200	1316±880
J0754+4950A	SDSS	4	DA	6	6710±340	7.39±0.82	133±55	0.328±0.326	1603±1090
J1254-0218A	SDSS	7	DA	92	17260±260	8.11±0.05	120±5	0.681±0.027	151±14
J1254-0218A	VLT	5	DA	8,8	15510±250	7.97±0.05	119±4	0.598±0.027	170±16
J2115-0741A	SDSS	5	DA	27	8090±130	8.13±0.09	68±5	0.675±0.057	1264±198
J2332+4917A	SDSS	6	DA	20	18490±450	7.99±0.07	400±21	0.614±0.041	93±17
Contaminants ^h									
J2124-1620A	APO	...	non-WD
J2124-1620B	APO	5	DA	19	10290±180	8.06±0.09	127±8	0.640±0.055	611±85

^a Objects with more than one listed S/N indicate multiple spectra were used to fit for the WD parameters.

^b The DB WDs in our spectroscopic sample were fit by P. Bergeron (pers. communication).

^c Confirming the nature of the non-DA WDs in these pairs requires higher S/N spectra.

^d Spectroscopic data for PG 1258+593A were taken from Gianninas et al. (2011). For a detailed discussion on this system see Girven et al. (2010).

^e J0748+3025 and J2259+1404 have already been identified as DA+DAH pairs (see Baxter et al. 2014, and references therein). J0748+3025 is composed of a pair of WDs separated by $\approx 1''5$. However, the SDSS spectrum shows three cores in H β ; see Figure 24.

^f Farihi et al. (2005) identified the companion to G 21-15 as a DC WD.

^g Silvestri et al. (2006) identified J2047+0021B as an unresolved binary composed of a carbon atmosphere WD (DQ) with a K7 companion.

^h J2124-1620 is composed of a DA WD and an A star.